Author Manuscript

Author Manuscript

Author Manuscript

Author Manuscript

HHS Public Access

Author manuscript

Neurobiol Dis. Author manuscript; available in PMC 2025 May 12.

Published in final edited form as:

Neurobiol Dis. 2024 December ; 203: 106732. doi:10.1016/j.nbd.2024.106732.

Developmental and physiological impacts of pathogenic human huntingtin protein in the nervous system

Tadros A. Hana[a], **Veronika G. Mousa**[a], **Alice Lin**[b], **Rawan N. Haj-Hussein**[a], **Andrew H. Michael**[a], **Madona N. Aziz**[a], **Sevinch U. Kamaridinova**[a], **Sabita Basnet**[a], **Kiel G. Ormerod**[a,*]

[a]Middle Tennessee State University, Biology Department, Murfreesboro, TN 37132, United States of America

[b]Brown University, Neuroscience Graduate Program, Warren Alpert Medical School, Providence, RI 02906, United States of America

Abstract

Huntington's Disease (HD) is a neurodegenerative disorder, part of the nine identified inherited polyglutamine (polyQ) diseases. Most commonly, HD pathophysiology manifests in middle-aged adults with symptoms including progressive loss of motor control, cognitive decline, and psychiatric disturbances. Associated with the pathophysiology of HD is the formation of insoluble fragments of the huntingtin protein (htt) that tend to aggregate in the nucleus and cytoplasm of neurons. To track both the intracellular progression of the aggregation phenotype as well as the physiological deficits associated with mutant htt, two constructs of human HTT were expressed in the *Drosophila melanogaster* nervous system with varying polyQ lengths, non-pathogenic-htt (NP-htt) and pathogenic-htt (P-htt), with an N-terminal RFP tag for *in vivo* visualization. P-htt aggregates accumulate in the ventral nerve cord cell bodies as early as 24 h post hatching and significant aggregates form in the segmental nerve branches at 48 h post hatching. Organelle trafficking up- and downstream of aggregates formed in motor neurons showed severe deficits in trafficking dynamics. To explore putative downstream deficits of htt aggregation, ultrastructural changes of presynaptic motor neurons and muscles were assessed, but no significant effects were observed. However, the force and kinetics of muscle contractions were severely affected in P-htt animals, reminiscent of human chorea. Reduced muscle force production translated to altered locomotory behavior. A novel HD aggregation model was established to track htt aggregation

This is an open access article under the CC BY-NC-ND license (http://creativecommons.org/licenses/by-nc-nd/4.0/).

*Corresponding author. kielormerod@gmail.com (K.G. Ormerod).

CRediT authorship contribution statement

Tadros A. Hana: Writing – review & editing, Writing – original draft, Investigation, Formal analysis, Data curation, Conceptualization. **Veronika G. Mousa:** Writing – review & editing, Methodology, Investigation, Formal analysis, Data curation. **Alice Lin:** Writing – review & editing, Methodology, Investigation, Formal analysis, Data curation. **Rawan N. Haj-Hussein:** Writing – review & editing, Methodology, Investigation, Formal analysis, Data curation. **Andrew H. Michael:** Writing – review & editing, Methodology, Investigation, Formal analysis, Data curation. **Madona N. Aziz:** Writing – review & editing, Methodology, Investigation, Formal analysis, Data curation. **Sevinch U. Kamaridinova:** Writing – review & editing, Methodology, Investigation, Formal analysis, Data curation. **Sabita Basnet:** Investigation, Data curation. **Kiel G. Ormerod:** Writing – review & editing, Writing – original draft, Visualization, Validation, Supervision, Software, Resources, Project administration, Methodology, Investigation, Funding acquisition, Formal analysis, Data curation, Conceptualization.

Declaration of competing interest

The authors declare that they have no known competing financial interests or personal relationships that could have appeared to influence the work reported in this paper.

Author Manuscript Author Manuscript Author Manuscript Author Manuscript

throughout adulthood in the wing, showing similar aggregation patterns with larvae. Expressing P-htt in the adult nervous system resulted in significantly reduced lifespan, which could be partially rescued by feeding flies the mTOR inhibitor rapamycin. These findings advance our understanding of htt aggregate progression as well the downstream physiological impacts on the nervous system and peripheral tissues.

Keywords

Drosophila; Huntington's disease; Organelle trafficking; Neuromuscular junction; Aggregation

1. Introduction

Huntington's Disease (HD) is an inherited, autosomal dominant neurodegenerative disorder affecting 1/10,000–1/20,000 people in the US annually (Roos, 2010). HD is part of a broader family of polyQ disorders, which include Machado-Joseph Disease, the five spinocereberal ataxis types (1, 2, 6, 7, 17), spinal-bulbar muscle atrophy X-linked type 1 and dentatorubral pallidoluysian atrophy (La Spada and Taylor, 2003; Orr and Zoghbi, 2007). PolyQ disorders are linked to a pivotal expansion of a trinucleotide cytosine–adenine–guanine (CAG) repeat encoding a polyQ (Q: amino acid glutamine) tract in the coding region of causative genes (Fan et al., 2014). Clinically, polyQ disease patients experience progressive increases in loss of motor control, cognitive decline, and psychiatric disturbances (Paulson et al., 2017; Bates et al., 2015; Ross et al., 2014) In each disease-case, expansion of the polyQ region within the protein leads to protein aggregation; and although many of the disorders develop from mutations of unrelated genes, they share molecular and clinical characteristics (Wright et al., 2019; Holmes et al., 1999; La Spada et al., 1992; Ross, 1997; Cohen-Carmon and Meshorer, 2012).

HD is linked to a CAG expansion within exon 1 of the IT15/Huntington gene (The Huntington's Disease Collaborative Research Group, 1993). Expansion of the CAG repeat leads to expansion and increased length of the PolyQ region of the huntingtin protein (htt); greater expansion leads to earlier disease onset and greater penetrance of disease pathology (Kremer et al., 1994; Walker, 2007; Quarrell et al., 2012). While the htt protein is ubiquitously expressed, expanded CAG homorepeat mutations exert their pathology almost exclusively on neuronal tissue (Sharp et al., 1995). Critically, the pathophysiology of HD is linked to protein fragmentation leading to the formation of insoluble inclusion bodies (aggregates). These aggregates are observed throughout neurons commonly in the nucleus, cytoplasm, and axons (Landles et al., 2010; Perutz et al., 1994). In its early stages, HD displays preferential expression in the striatum, specifically increased neurodegeneration targeting medium spiny neurons in stages designated 1 through 4 (Gutekunst et al., 1999a; Waldvogel et al., 2015; Tabrizi et al., 2022). Interestingly, only 1–4 % of striatal neurons display aggregation, potentially due to the neuroprotective effects of the full length htt protein (Kuemmerle et al., 1999a). In contrast, aggregation is observed more often in other neuron types such as cortical and cerebellar when compared to striatal (Tagawa et al., 2004). Importantly, N-terminal htt fragments have been found to aggregate and exert pleotropic toxic effects on neurons (Landles et al., 2010; Juenemann et al., 2011; Podvin et al., 2022;

Author Manuscript Author Manuscript Author Manuscript Author Manuscript

Pircs et al., 2018; Chang et al., 2006; Chen et al., 2023). In particular, proteolysis of htt at the caspase-6 cleavage site is a critical event in mediating neuronal dysfunction and neurodegeneration (Graham et al., 2006a). Of the numerous other defects, htt aggregation is well known to lead to deficits in axonal trafficking (Trushina et al., 2004; Weiss and Littleton, 2016). However, the downstream implications of htt aggregation in neuronal and neuromuscular structures and function remain poorly understood. Therefore, understanding the developmental proliferation of htt fragment aggregation and putative downstream implications will lead to a better comprehension of HD progression and pathophysiology.

Herein, we exploited the extensive genetic and molecular toolkits in *Drosophila* to investigate the progression of htt fragment aggregation using pathogenic and non-pathogenic polyQ constructs truncated at the caspase-6 cleavage site with an RFP tag for *in vivo* visualization to accurately model the behavior of mutant htt. This model facilitates *in vivo* htt-aggregation tracking in the central and peripheral nervous systems to elucidate the progression of their formation. Combining fluorescently tagged htt-constructs and fluorescently tagged-organelles (synaptotagmin-1 and Brain Derived Neurotrophic Factor-GFP generated here) demonstrated profound impacts of htt-aggregates on the trafficking dynamics of synaptic vesicles and dense core vesicles *in vivo*. Htt-aggregates did not appear to alter neuromuscular junction morphology, however, excitation-contraction coupling in larvae expressing pathogenic htt was severely impaired, which translated to locomotor deficits. To generate greater longitudinal studies, the htt-constructs were successfully expressed in the adult wing, which showed a similar aggregation profile to larvae. Lastly, to explore the cellular pathways underlying the proliferation of htt-aggregates, the mTOR pathway was targeted using rapamycin-supplemented diet in adults, resulting in a significant increase in lifespan of the flies expressing pathogenic htt in the nervous system.

2. Materials and methods

Husbandry.

Drosophila melanogaster were cultured on standard medium at 22 °C at constant humidity on a 12:12 light:dark cycle. Fly lines were obtained from the Bloomington *Drosophila* Stock Center (BDSC), see Table 1. UAS-htt-Q15, UAS-htt-Q138, and UAS-Syt1-GFP fly lines were generously provided by Troy Littleton, Massachusetts Institute of Technology.

Generation of transgenic construct.

cDNA of preproBDNF-eGFP (BDNF-eGFP) was subcloned into pUAST vector. cDNA of mouse preproBDNF was kindly provided by Prabhodh Abbineni (Loyola University Chicago). Microinjection of constructs was performed by BestGene Inc. to generate transgenic *Drosophila* strains.

2.1. Larval htt aggregation imaging

Egg-laying assay. Three (3) adult males and three (3) adult females were isolated the day of eclosion and mated in a separate food vial. On day 3, the flies were transferred to an egg-laying assay which included a 35 mm petri dish with grape agar and yeast paste. Flies were left for 24 h to lay eggs, and afterwards, unhatched eggs were transferred onto

Author Manuscript Author Manuscript Author Manuscript Author Manuscript

a new food plate (Michael et al., 2024). Newly hatched larvae were collected and isolated on separate dishes at two-hour intervals. Larval age was measured as hours after hatching (HAH).

Transcutaneous (intravital) imaging (24, 48, and 72 HAH). Larvae were transferred from food vials to microscope slides. Clear tape was applied to slides, creating a small channel with dimensions matching the height and width of the larvae. Larvae were then coated with a layer of glycerol and a cover slip was placed on top. Slides were refrigerated at 4 °C for three-to-five minutes to fully immobilize the larvae prior to imaging.

Dissected preparations (96 and 120 HAH). Early and late third-instar larvae were dissected in HL3.1 calcium-free saline with the following composition (in mM): NaCl: 70; KCl: 5; $CaCl_2$:0; $MgCl_2$: 4; $NaHCO_3$: 10; Trehalose: 5; Sucrose: 115; HEPES: 5, (pH = 7.18) (Feng et al., 2004). All images were taken with a Nikon Eclipse microscope, equipped with a Lumencor Fluorescence Light Engine, Hammamatsu Orca-fusion camera, and processed using Nikon Elements software. All images were taken with a 60× water-immersion objective.

Analysis: To determine aggregate thresholds, RFP-positive puncta were recorded live from the segmental nerve branches (SNB) of five (5) different Elav > NP-htt larvae at 25 frames per second (fps). From the five (5) animals, a total of 25,000 μm of nerves were assessed to identify the largest motile aggregate, found to be 1.8 μm^2. Consequently, for analysis the size threshold was set at 150 % of 1.8 μm^2 (2.7 μm^2) and the fluorescence intensity threshold to 2 SD above background.

First- and second- instar image analysis. All data were obtained using the ROI feature on Nikon Elements. The ventral nerve cord (VNC) was identified by the presence of the neuropil. Fluorescence intensity was extrapolated by manually tracing around the VNC. For SNB analysis, at least 500 μm of nerves were imaged from each preparation, and aggregates forming in the motor neuron (MN) axons were manually selected and traced. Number, average fluorescence intensity, and size were all measured from the aggregates in each ROI and measurements were exported to Excel.

Early- and late- third instar (96 and 120 HAH). All data were obtained using the ROI feature on Nikon Elements. The VNC was identified by the presence of the neuropil or by tracing the SNBs to their origin point. SNBs were imaged 450 μm downstream of the brain, and each preparation had a minimum of ten (10) individual nerve branches to be analyzed. Number, average fluorescence intensity, and size were all measured from the aggregates in each ROI and measurements were exported to Excel.

Morphological Measurements: Twenty (20) randomly selected wandering third-instar larvae from each genotype were selected and rinsed in deionized water prior to being measured. Larvae were pinned on the posterior and anterior ends using minuten pins and stretched until abdominal contractions were no longer observed. Length, at the longest points, and width, at the widest points, were recorded using a dissection microscope

Author Manuscript Author Manuscript Author Manuscript Author Manuscript

equipped with an objective reticule. Area was calculated as the product of length times width.

Organelle trafficking. Wandering larvae were isolated from their respective vials and dissected in standard HL3.1 saline. Live imaging of third-instar larval SNB was performed using UAS-Syt1-GFP (SV) and UAS-BDNF-GFP (DCV) in both the pathogenic- (P) and non-pathogenic-(NP) htt backgrounds. 90 s videos were recorded at 4 fps on a Zeiss Axio Imager 2 equipped with a spinning-disk confocal head (CSU-X1; Yokagawa) and ImagEM X2 EM-CCD camera (Hammamatsu). An Olympus LUMFL N 60× water-immersion objective with a 1.10 NA was used to acquire images. All videos were acquired at the same fps and laser intensity. Velocity 3D Image Analysis software (PerkinElmer) was used to analyze images. Kymographs were extracted and analyzed using Kymograph Clear and Kymograph Direct.

Immunohistochemistry. Wandering third-instar larvae were dissected in hemolymph-like saline HL3.1. The larvae were fixed for three minutes in 4 % paraformaldehyde and subsequently washed in phosphate-buffered saline (PBS), with 0.05 % Triton X-100 (PBST), and blocked with 5 % BSA. Larvae were then incubated with antibodies in PBST at room temperature for 2 h and washed three times for 15 min in PBST. Finally, larvae were mounted in a medium containing DAPI (ab104139). Antibodies used for this study include the following: DyLight 649 conjugated anti-horseradish peroxidase (HRP), 1:500 (catalog #123–605–021, Jackson ImmunoResearch) and the filamentous actin probe, phalloidin conjugated to Alexa Fluor™ 488 (A12379, Thermo). Immunoreactive proteins were imaged on the Nikon fluorescence microscope (see above) using either 20× air or 60×-water immersion objectives and processed using Nikon Elements software.

Neuromuscular junction analysis: NMJ analysis was performed using a horseradish peroxidase (HRP) stain. Innervation length was obtained using a distance measurement feature on Nikon Elements to measure the extent of innervation on the surface of muscle fiber 4. Bouton number and fluorescence values for each genotype were calculated using regions of interest (ROI) tool in Nikon Elements, by manually selecting and tracing HRP-positive boutons. Average bouton fluorescence and area from each ROI were exported from the software and bouton number and area were subsequently exported to excel.

Muscle Examination: Length and width of individual muscles were quantified using the distance measurement feature on Nikon Elements. Muscles from abdominal segments A3-A5 were used. Muscle length was measured along the middle of muscle fiber 4, using the midpoint of the muscle insertion point on either end of the muscle. Muscle width was measured across the midline of the muscle, equidistant from both muscle insertion points. The product of both length and width were used to compute muscle area. Muscle sarcomere length was measured using the intensity profile function in Nikon Elements software to produce a sinusoidal graph of anti-actin fluorescence intensity. The length of the sarcomere was then measured as a single sinusoidal wavelength. Moreover, I-band was obtained by measuring the width of each peak from the first significant decrease in fluorescence (Michael et al., 2024). Fixed dissections were mounted onto microscope slides with DAPI

Author Manuscript Author Manuscript Author Manuscript Author Manuscript

mounting media (ab104139). Nuclei area was measured from overlayed images of DAPI and anti-actin using a region of interest (ROI) measuring tool on Nikon Elements. Subsequent fluorescence intensity, number, and area of each ROI was then exported to Microsoft Excel. Inter-nuclei distance was obtained by taking the three most central nuclei and measuring the three closest nuclei to them.

Muscle force recordings: Force recordings were conducted as described in Ormerod et al., 2022 (Ormerod et al., 2022). Briefly, third-instar larvae were pinned dorsal side up and a lengthwise cut was made along the dorsal midline. Submerged in modified HL3.1 saline (4 mM Mg and 1.5 mM Ca^{2+}), the preparation was eviscerated and the CNS was removed. Segmental nerve branches were stimulated using a suction electrode and A.M.P.I. Master 8 stimulator. Force recordings were acquired using the Aurora Scientific 403 A Force Transducer System, which includes a force transducer head stage, amplifier, and digitizer. Contractions were elicited using 5×10^{-4} s impulses for 600 ms, with an interburst duration of 15 s, with varying intraburst stimulation frequencies (1–150 Hz). Every preparation was visually inspected to ensure at least 5 abdominal segments were stimulated. Digitized data was acquired using Aurora Scientific Software, Dynamic Muscle Acquisition (DMCv5.5). Digitized data were imported and processed in MATLAB using custom code (Ormerod et al., 2022).

Electrophysiology. Wandering third-instar larvae were isolated from their vials and rinsed with DI H2O. Standard dissection protocol was followed (Jan and Jan, 1976), and preparations were bathed in HL3.1 (0.25 mM Ca^{2+}) (Feng et al., 2004). Larvae were pinned dorsal side up and motor nerve branches were stimulated (A.M.P.I. Master 8) using a suction electrode following removal of the CNS. All animals were stimulated at 0.2 Hz and intracellular voltage was recorded using a sharp recording electrode (40–60 MΩ) from muscle fiber 6, in abdominal segments A3-A5. Voltage traces were digitized using a Minidigi 1B (Molecular Devices) and visualized using Axoscope (Molecular Devices) Software. Excitatory junctional potentials (EJPs) and miniature excitatory postsynaptic potentials (minis) were quantified using ClampFit, and data were explored to Microsoft Excel for data compilation, and subsequently to GraphPad prism for statistical analysis and figure making.

Larval Crawling. Third-instar wandering larvae were isolated from fly vials and washed seven times in DI water. Groups of 10 larvae from the same genotype were transferred to the center of a 1 % agar plate for a 5-min crawling session. 10 separate recordings of 10 larvae per recording were taken for each genotype assessed. Recordings of 10 larvae per genotype were made using an infrared camera housed inside a 24”×24”×24” black box. Videos were processed using SpinView and subsequently converted to an Interoperatory Master Format (IMF) file. Caltech Multiple Fly Walking Tracker (CTRAX) software extracted a CSV file with X and Y coordinates and heading in radians. Excel scripts analyzed the data for distance per frame, displacement, velocity per 0.5 s, and angular velocity, revealing genotype-specific locomotor traits.

Author Manuscript Author Manuscript Author Manuscript Author Manuscript

Adult Lifespan Assay: For each genotype, 400 total flies were tracked daily from eclosion to death. The 400 flies were divided into separate vials of 20 flies, each with 10 female and 10 males, isolated upon the day of eclosion. Once per week, the flies were transferred to fresh food vials. Each vial was incubated at 22 °C and examined daily by counting the number of nonviable flies and the sex.

Rapamycin. Standard fly food was prepared with Rapamycin (Medchemexpress) dissolved in 1 mL of dimethylsulfoxide (DMSO). 400 adult P-Htt flies were separated into 20 separate vials containing 10 males and 10 females. Adults were isolated within a 24-h window post eclosion and designated as day 1 old. Flies were transferred to rapamycin-containing food as indicated in the legend of Fig. 10. Flies were tracked every day and transferred to fresh food vials every five days. The number and sex of nonviable flies each day were counted, and the data were input into Microsoft Excel.

Wing imaging. Imaging was performed every 5 days for 50 days. At each timepoint, adult flies were removed from food vials and transferred to a CO_2-pad. Wings were removed *via* cutting the hinges and visualized under a dissection microscope. The wings were mounted on a microscope slide with glycerol. Wings were imaged using the same Nikon microscope as above, and a 60× oil objective. The entirety of L1 of each wing was imaged and then stitched together using Nikon Elements Software. After imaging, Nikon Elements Software was used to select non-motile aggregates using a threshold of 2.7 μm^2 and a fluorescence intensity 2 SD above the background.

Statistical analysis. GraphPad Prism 10.3.0 was used for statistical analysis. Appropriate statistical metrics were performed for each dataset along with the F, and P statistics. Statistical comparisons were made with controls unless noted. Appropriate sample size was determined using a normality test. Data are presented as the mean ± SEM unless otherwise stated (*$p < 0.05$, **$p < 0.01$, ***$p < 0.001$, n.s. = not significant).

3. Results

3.1. Htt aggregation does not impact development or gross morphology in third-instar larvae

Given that huntingtin (htt) intracellular protein aggregation is a progressively occurring event in HD, the effects of pathogenic *versus* non-pathogenic human htt expression on the growth and development of *Drosophila melanogaster* were initially investigated. Using the Gal4/UAS system, *Drosophila* expressing either a non-pathogenic polyQ tract of 15 repeats (NP-htt), or a pathogenic polyQ tract of 138 repeats (P-htt) corresponding to a juvenile form of HD, within the human HTT gene, under the control of UAS were investigated (Weiss et al., 2012). Both constructs contain a fused N-terminal red fluorescent protein (RFP) to enable *in vivo* visualization and analysis of the formation and localization of htt. Given that proteolysis of full length htt leads to aggregate formation, we employed a truncated form of htt at the caspase-6 cleavage site comprising the initial 588 amino acids to accurately model the aggregation phenotype (Graham et al., 2006a; Weiss et al., 2012). To selectively examine htt progression within the nervous system (NS), both transgenic lines were crossed with

Author Manuscript Author Manuscript Author Manuscript Author Manuscript

the neuronal driver Elav-Gal4 (Elav). To fully characterize the effects of P-htt expression on the growth and development of *Drosophila* initially, each stage of development was examined. Initially, an egg-laying assay was conducted using 3 males and 3 females (Fig. 1). After 24 h, the total number of eggs were counted for both transgenic lines expressed in the NS (Elav > NP, Elav >P) as well as control lines (Elav, UAS-NP-htt, and UAS-P-htt); no statistical differences were observed (Fig. 1 A, C. One-way ANOVA, F = 1.3, P = 0.31). Next, the number of eggs that hatched into first instars were counted; no statistical differences were observed between genotypes (Fig. 1 D, One-way ANOVA, F = 0.87, P = 0.49). Subsequently, 20 third-instar larvae for each genotype were collected and placed into separate vials (Fig. 1B). No significant differences were observed in percentage of larvae that underwent pupation between the 5 genotypes (Fig. 1 E, One-way ANOVA, F = 3.41, P = 0.08). Lastly, the percentage of larvae eclosed revealed significant differences between Elav > NP-htt and Elav > P-htt, as well as between Elav > NP-htt and NP-htt (Fig. 1 F, One-way ANOVA, F = 4.65, P = 0.008). Taken together, expression of P-htt in the nervous had no impact on development until the adult stage.

To further assess the potential impacts of htt-aggregation on growth and development, an assessment of third-instar larvae expressing P-htt or NP-htt, gross larval morphology was conducted (Fig. 1 G). Twenty randomly selected third-instar larvae from each of the 5 genotypes were measured and no significant differences in larval length (Fig. 1 H, One-way ANOVA F = 0.75, P = 0.56), width (Fig. 1 I, One-way ANOVA, F = 1.33, P = 0.26), or area (Fig. 1 J, One-way ANOVA, F = 1.13, P = 0.35) were observed. These results suggest that htt-expression in the nervous system does not impact developmental timing or gross morphology.

3.2. P-htt aggregates significantly increase in size, number, and fluorescence intensity between 24 and 72 h post egg hatching

Having demonstrated that htt-expression in the NS does not impact developmental timing or gross morphology, an examination of cellular P-htt progression within individual neurons was conducted. Given the semi-transparent nature of first and second instar larvae, we were able to perform transcutaneous imaging from fully intact, undissected animals (Akbergenova et al., 2018). To precisely track the progression and proliferation of htt-aggregation, eggs were collected every 2 h and sorted into separate fly vials facilitating a precise 2-h window for developmental tracking based on hours after hatching (HAH). First instar larvae were imaged transcutaneously for htt expression in the NS using the Elav driver, which expresses prolifically in motor neurons (Noordermeer et al., 1994). In Elav > NP-htt larvae at 24 HAH, no quantifiable RFP expression was observed in the ventral nerve cord (VNC) when measuring the average fluorescence intensity of the entire VNC relative to background (VNC, Fig. 2 Ai, C). At 48HAH, a significant increase in RFP fluorescence was observed in Elav > NP-htt larvae, but no further significant increase was observed for 72, 96, or 120 HAH compared to the 48 H timepoint (Fig. 2 Aii–v, C, One-way ANOVA, P > 0.05). For Elav > P-htt larvae, quantifiable RFP fluorescence was observed in the VNC 24HAH, significantly greater than Elav > NP-larvae of the same age (Fig. 2 Avi, C, One-way ANOVA, F = 85.99, P < 0.0001). A day later, in 48 HAH Elav > P-htt larvae, significantly more htt-aggregation was observed compared to 24 H (Fig. 2 Avi–vii, C, P < 0.01). At 72

Author Manuscript Author Manuscript Author Manuscript Author Manuscript

HAH, significantly more fluorescence was observed compared to both 24 and 48 HAH (Fig. 2 Avi–viii, C, P < 0.01); however, 96 and 120 HAH timepoints did not show any differences compared to 72 HAH (Fig. 2 Aviii–x, C). Thus, in Elav > P-htt larvae, htt-aggregation steadily accumulated in the VNC from 0 to 72 HAH, however, no further htt-proliferation was observed after 72 HAH (Fig. 2 Avi–x, C). Conversely, quantifiable RFP fluorescence was not observable until 48 HAH for Elav > NP-htt larvae, and no significant further increases in fluorescence was observed thereafter (Fig. 2 Ai–v, C).

To track the progression of P-htt aggregation in neurons more thoroughly, the main segmental nerve branches (SNB) projecting from the VNC were imaged (Fig. 2 B). These nerves contain axons projecting to body-wall muscles (Jan and Jan, 1976). No detectable htt-aggregates were observed in the SNBs of Elav > NP-htt larvae until 120 HAH (Fig. 2 Bi–v, D, One-way ANOVA, F = 104.2, $P < 0.0001$). For Elav > P-htt larvae, no htt-aggregation was observed 24 HAH; however, a prolific increase in the number of aggregates, quantified per 100 μm of SNB, was observed 48 HAH (Fig. 2 Bvii, D). Subsequently, the 72HAH timepoint did not show a significant increase compared to 48 HAH, but the 96 and 120 HAH timepoints revealed a significant increase compared to 48 HAH, reaching a plateau in aggregate number per 100 μm after 96 HAH (Fig. 2 Bviii–x, D). Statistical differences were observed between the Elav > NP-htt and Elav > P-htt larvae at the 48, 72, 96, and 120 HAH timepoints (Fig. 2 D, One-way ANOVA). To examine quantifiable differences between Elav > NP-htt and Elav > P-htt expressing in larvae, a comparison of the two genotypes was conducted at the 120 HAH timepoint. Every SNB aggregate was plotted as a function of its size to demonstrate the profound differences in both number and size (Fig. 2 E). Next, each aggregate was plotted as a function of its fluorescence intensity (Fig. 2 F). Significant differences were observed between Elav > NP-htt and Elav > P-htt larvae at 120 HAH in the average aggregate size (Fig. 2 G, NP: 5.6 ± 3.1, P: 11.2 ± 3.2, *t*-test, $t = 2.8$, $P = 0.02$) and average fluorescence intensity (Fig. 2 H, NP: 401.7 ± 36.2, P: 2248.2 ± 984.7, t-test, $t = 4.2$, $P = 0.003$). Collectively, these results demonstrate a prolific increase in htt-aggregates from the pathogenic construct beginning as early as 24 HAH in the VNC, and 48 HAH in the axons, while comparatively few htt-aggregates are present in the VNC or motoraxons in the non-pathogenic construct.

3.3. Htt aggregates severely impact axonal synaptic vesicle trafficking

To assess the impact of htt-aggregates on motor neuron (MN) morphology and physiology, we first explored the trafficking of organelles within the SNBs using *in vivo* live imaging. Given that MNs are glutamatergic, an assessment of the impact of aggregation on trafficking of synaptic vesicles (SVs) containing the neurotransmitter (NT) glutamate was conducted by expressing a genetically-encoded GFP-tagged version of synaptotagmin 1 (UAS-Syt1-GFP), the well-characterized calcium-sensor for SV-fusion (Fig. 3 A) (Yoshihara and Littleton, 2002; Lee and Littleton, 2015; Littleton et al., 1993). SV flux (number/min) within the SNB was calculated for Elav > UAS-Syt1-GFP (10.7 ± 3.3, Fig. 3 C). Expressing this construct in the NP-htt background did not significantly alter SV flux (10.5 ± 3.8, Fig. 3 C, One-way ANOVA, F = 27.5, $P > 0.05$). However, when examining the impact of SV flux in flies also expressing P-htt, SV trafficking was significantly impaired (4.7 ± 2.0, Fig. 3 C, One-way ANOVA, F = 27.5, $P < 0.0001$). To directly examine the impact of htt-aggregation on

Author Manuscript Author Manuscript Author Manuscript Author Manuscript

trafficking, SV flux was calculated up- and downstream of SNB with aggregates exceeding 5 μm^2 (Fig. 3 B). Upstream of an htt-aggregate, SV trafficking was significantly impaired compared to both Elav-Gal4 > UAS-Syt1-GFP, and Elav-Gal4 > UAS-Syt1-GFP, NP-htt (Fig. 3 B, C). A kymograph depicts the unco-ordinated, back and forth movement of GFP-positive puncta (SVs) upstream (*a*-anterior, *p*-posterior) of a htt-aggregate, and a dramatic reduction in SV movement downstream (Fig. 3 Biii). Impact of htt-aggregation in P-htt animals on SV trafficking was most apparent downstream, and significantly different from upstream activation as well as from SV trafficking in NP-htt animals (1.4 ± 0.9, Fig. 3 C, Oneway ANOVA, F = 27.5, P < 0.0001). To localize htt-aggregation more precisely within individual MNs, we attempted to examine the impacts of trafficking within single axons by using MN-Ib-Gal4 and MN-Is-Gal4 drivers (Fig. 3 D) (Aponte-Santiago et al., 2020). However, neither driver was strong enough to visualize both htt-aggregates and SV trafficking simultaneously. The number of htt-aggregates in individual axons within SNB, observable with the single MN-driver, MN-Ib-Gal4 > P was comparable to what was observed using Elav (Data not shown).

3.4. Trafficking of neuropeptides is significantly impaired by P-Htt aggregates

To further examine the impacts of htt-aggregates on axonal trafficking, we examined the effect on dense core vesicle (DCV) trafficking. DCVs are considerably larger (2–3×) than SV in diameter, and have a dark and granulated core on electron micrographs, resulting from dense packing of their cargo, which can contain numerous cell-signaling and regulatory components including neuropeptides, peptide hormones, growth factors, signaling proteins, biogenic amines and active zone components (Kuznetsov and Kuznetsov, 2017; Gondré-Lewis et al., 2012; Salio et al., 2007; Hummer et al., 2017; Cunningham and Littleton, 2022; Ormerod et al., 2013). Evidence suggests that transport deficits of BDNF are key contributors to HD (Szebenyi et al., 2003; Gauthier et al., 2004). Consequently, we created a novel DCV overexpression line tagged with GFP, using traditional cloning techniques incorporating the UAS-system, to overexpress the neuropeptide brain-derived neurotropic factor (UAS-BDNF-GFP, Fig. 3 E). The molecular weight of the construct plus GFP was validated using a Western blot. Kymographs were created to calculate the trafficking metrics of BDNF-tagged DCVs in SNBs, including velocity, flux, and duty cycle. NS expression of BDNF-GFP using Elav-Gal4 revealed a baseline flux calculation of 30.5 ± 3.6 (Fig. 3 F). Trafficking of DCVs was significantly impaired in Elav-Gal4 > UAS-BDNF-GFP, NP-htt compared to Elav-Gal4 > UAS-BDNF-GFP (Fig. 3 F, One-way ANOVA, F = 101.1, $P > 0.05$). However, DCV trafficking was significantly reduced when P-htt was expressed (Fig. 3 F, One-way ANOVA, F = 101.1, $P < 0.001$). As observed for SV trafficking, DCV trafficking was impaired to a greater extent downstream of htt-aggregates compared to upstream (Fig. 3 F). These results demonstrate that axonal trafficking is significantly reduced only in the presence of P-htt aggregates, and not NP-htt aggregates. Moreover, the effects of htt-aggregates on organelle trafficking are most dramatically reduced downstream of htt-aggregates.

3.5. Htt aggregates do not impair proper neuromuscular junction formation

Following the observation that organelle trafficking was significantly impaired in P-htt axons, we next sought to examine the downstream or developmental effects of htt-

Author Manuscript Author Manuscript Author Manuscript Author Manuscript

aggregations. The *Drosophila* larval glutamatergic neuromuscular junction (NMJ) has served as an invaluable model glutamatergic synapse for over half a century (Jan and Jan, 1976). To establish if htt-aggregation was visible at the NMJ, wholemount immunohistochemical stains for RFP and HRP were conducted. Htt-aggregates were not detected at the NMJ of Elav > NP-htt third-instar larvae (Fig. 4 Ai). In the 8 immunostains conducted for Elav > P-htt third-instar larvae, aggregates were observed at the NMJ innervating muscle fiber (MF) 4 at a single NMJ in MF 4 (Fig. 4 Aii). Of note, htt-aggregates were often observed at branching points upstream of the NMJ (data not shown). The total length of MN innervation along the surface of MF 4, a large, flat muscle ideal for NMJ morphology assessments, was measured (Fig. 4 A). No significant difference was observed between Elav > NP-htt and Elav > P-htt expressing lines (Fig. 4 B, Oneway ANOVA, $F = 41.1$, $P > 0.05$). Two morphologically and physiologically distinct MN-subtypes, MN-Ib (tonic-like) and MN-Is (phasic-like), are located at the larval NMJ. A separate assessment of each MN-subtype was conducted to isolate MN-specific effects of htt-aggregates on innervation length, but no significant differences were observed (Fig. 4 B). Next, an assessment of the total bouton number, along with a separation of bouton number per MN-subtype was conducted and no significant differences were observed (Fig. 4 C). Lastly, an assessment of the number of active zones (AZs) per bouton was also calculated using an immunostain against a member of the ELKS-family of scaffolding proteins - bruchpilot (brp, Fig. 4 Aiii) - and no significant difference between Elav > NP-htt and Elav > P-htt expressing lines was observed (data not shown). Taken together, Elav > NP-htt nor Elav > P-htt expressing lines had any observable effects on NMJ presynaptic structural morphology.

3.6. Htt aggregates did not demonstrate deficits in synaptic transmission at low frequency stimulation

Although no morphological deficits were observed at the NMJ, electrophysiological recordings were conducted to examine the physiological impacts of NP- and P-htt expression at the NMJ (Fig. 5). Unstimulated, sharp-intracellular recordings were initially performed to examine changes in miniature excitatory junctional potential (minis) amplitude and frequency (Fig. 5 A). No significant change in mini amplitude was observed between control (Elav), Elav > NP-htt, and Elav > P-htt lines (Fig. 5 C, One-way ANOVA, $F = 2.8$, $P > 0.05$). There was also no significant change in mini frequency between the control, Elav > NP-htt, and Elav > P-htt lines (Fig. 5 D, One-way ANOVA, $F = 0.7$, $P > 0.05$). Next, low frequency stimulation was applied to severed SNBs *via* a suction electrode at 0.2 Hz to generate excitatory junctional potentials (EJPs, Fig. 5 B). Similar to the effects on minis, no significant deficits in the evoked release of synaptic vesicles were observed between control, Elav > NP-htt, and Elav > P-htt larvae EJPs (Fig. 5 E, One-way ANOVA, $F = 0.7$, $P > 0.05$). Collectively, our electrophysiological recordings do not demonstrate any physiological impacts of htt-aggregation on neuromuscular transduction.

3.7. The structure of larval body wall muscles was notimpacted by htt-aggregation

Next, an assessment of muscle morphology was conducted to examine changes in postsynaptic structure (Fig. 6). Immunohistochemical stains to examine changes in gross muscle structure were conducted using the actin-stain phalloidin (Fig. 6 A–D). Gross morphological assessments of muscle fiber (MF) 4 from third-instar larvae Elav, Elav >

Author Manuscript Author Manuscript Author Manuscript Author Manuscript

NP-htt, and Elav > P-htt were conducted and no significant differences were observed for MF length (Fig. 6 Dii, One-way ANOVA, F = 0.5, $P = 0.6$), MF width (Fig. 6 Diii, One-way ANOVA, F = 4.1, P > 0.05), and MF area (Fig. 6 Div, One-way ANOVA, F = 1.6, $P = 0.2$). To examine possible changes in postsynaptic ultrastructure, a fluorescence profile line feature was used within Nikon Elements to measure fluorescence peaks along a discrete line of a minimum length of 200 μm as a precise estimation of muscle sarcomere and I-band lengths (Fig. 6 Ei.) (Michael et al., 2024). Immunohistochemical stains from Elav > NP-htt and Elav > P-htt larvae did not show any significant changes in either sarcomere length (Fig Eiii, *T*-Test, $t = 0.46$, $P = 0.65$) or I-band length (Fig Eiv, *t*-test, $t = 0.82$, $P = 0.43$). Lastly, an immunostain using the nuclear stain DAPI was conducted to examine changes in muscle nuclei structure and morphology (Fig. 6 F). Stains from Elav > NP-htt and Elav > P-htt expressing larvae did not show any significant differences in nuclei number (Fig. 6 Fii, t-test, $t = 1.21$, $P = 0.26$), nuclei area (Fig. 6 Fiii, t-test, $t = 0.84$, $P = 0.40$), and internuclear distance (Fig. 6. Fiv, t-test, $t = 1.55$, $P = 0.13$). Collectively, there does not appear to be any post-synaptic effects of Elav > NP-htt or Elav > P-htt aggregation at the NMJ.

3.8. Muscle force production is significantly reduced in larvae expressing P-htt

The MNs contained within the SNBs projecting from the VNC transmit descending patterned outputs, driving muscle contraction in larval body-wall muscles responsible for larval peristalsis (Ormerod et al., 2022; Ormerod et al., 2013; Ormerod et al., 2015). To examine the impact of NP- and P-htt expression in the NS on mechanisms of the excitation-contraction coupling machinery, a force transducer system was used to measure changes in muscle force production from semi-intact larvae (Fig. 7 A). With the brain removed, the motor neurons were activated *via* electrical stimulation using a series of frequencies within the range commonly output from the VNC, to generate a force-frequency curve for each genotype ranging from 1 to 150 Hz (Fig. 7 B) (Ormerod et al., 2022). Elav > NP-htt third-instar larvae did not show any differences in muscle contraction compared to Canton S. controls, however, Elav > P-htt larvae had significantly reduced muscle force production (Fig. 7 C). The amplitude of contractions generated at 40 Hz were reduced by 34.6 ± 5.1 % in Elav > P-htt compared to Elav > NP-htt larvae (Fig. 7 C, *peak force*). Interestingly, the rise and decay time constants (Fig. 7 C, τ_{rise} and τ_{decay}) were also slower for Elav > P-htt compared to Elav > NP-htt or Canton S. controls (τ_{rise}: 33 ± 13 % increase, and τ_{decay}: 88 ± 31 % increase). Force frequency curves, generated in Fig. 7 Di (300 ms), show profound changes in muscle performance in Elav > P-htt expressing larvae compared to Elav > NP-htt and controls. Elav > P-htt larvae did not show any observable muscle contractions until the stimulation frequency exceeded 10 Hz, while observable contractions were elicited in Elav > NP-htt and Canton *S. larvae* at 1 Hz (Fig. 7 Di). A 30–39 % decrease in muscle force production was observed between 10 and 40 Hz, the aspect of the force-frequency curve with greatest plasticity (Ormerod et al., 2022). Contraction force was significantly reduced at all stimulation frequencies below 100 Hz that were examined between the two constructs (Fig. 7 Di). A well-documented leftward shift in the force-frequency curve is observed by increasing the duration of the intraburst stimulation (Ormerod et al., 2022). Figs. 7 Dii–iv, show force-frequency curves for larvae with 600, 750, and 900 ms duration simulation. By increasing the duration of the intraburst frequency, greater temporal summation occurs, resulting in greater larval force generation, and a steady decline in the differences in force

Author Manuscript Author Manuscript Author Manuscript Author Manuscript

production between Elav >NP-htt and Elav > P-htt expressing larvae. Despite this leftward shift, significant differences exist between Elav > P-htt and Elav > NP-htt from 10 to 40 Hz for all simulation durations (Fig. 7 D).

3.9. Human P-htt expression showed marked deterioration in larval crawling

Given the profound effects of P-htt expression on muscle contraction, an assessment of larval crawling was conducted to determine if alterations in muscle contraction biology manifested as changes in locomotor or crawling behavior. In sets of 10 larvae at a time, 100 larvae from each genotype were placed inside a box devoid of light, illuminated using infrared light, and recorded with a 2 MP infrared camera. Their crawling behavior was tracked using CTRAX software, and assessed for velocity and distance travelled (Fig. 8 A) (Branson et al., 2009). UAS-NP-htt, UAS-P-htt, Elav, and Elav > NP-htt larvae all displayed similar crawling behavior (Fig. 8 B, C, One-way ANOVA, $P > 0.05$). Larva expressing Elav > P-htt showed a significant reduction in crawling velocity compared the other 4 genotypes (Fig. 8 B, One-way ANOVA, $F = 36.63$, $P < 0.0001$). Elav > P-htt expressing larvae also showed a significant reduction in the distance travelled over a period of 30 s of continuous crawling (Fig. 8 C, One-way ANOVA, $F = 28.01$, $P < 0.0001$).

3.10. Htt expression in the wings of adult Drosophila reveal similar patterns to the larval NS

A limitation to using larvae as a model for investigations of neurodegeneration is their relatively short lifespan. To complement our current approach, we sought to develop a model to investigate cellular htt-aggregation across the lifespan of adult *Drosophila*. Expressing P-htt using Elav has previously been demonstrated to result in a significantly reduced adult lifespan (Weiss et al., 2012). Furthermore, imaging of htt-aggregation in the adult CNS is technically challenging. A screen for Gal4-drivers in the wing was conducted to circumvent both these obstacles, and appl-Gal4 was identified to express in the L1 vein of the wing (Fig. 9 A,) (Noordermeer et al., 1994). Adults expressing appl > NP-htt and appl > P-htt were isolated on the day of eclosion, and the right wing of unique animals were imaged transcutaneously every 5 days for 50 days. Small and infrequent aggregates were observed in the wings of appl > NP-htt adults while similarly sized, yet more numerous aggregates were observed in the wings of 5-day old appl > P-htt animals (Fig. 9 Bi, iv, C, D). For appl > NP-htt animals, no significant increase was observed for subsequent 5-day intervals from 5 to 50 days, indicating no significant increase the aggregate number (Fig. 9 C, One-way ANOVA, $F = 14.44$, $P = 0.0001$). For appl > P-htt animals, a significant difference was observed between day 5 and days 45–50, demonstrating a significant increase with age (Fig. 9 C). Most notably, a significant difference was observed in the number of htt aggregates between appl > NP-htt and appl > P-htt at each time-point, except day 10, showing significantly more htt-aggregates in the animals expressing the pathogenic construct (Fig. 9 C). For each aggregate, both the area and fluorescence intensity were also quantified (Fig. 9 D–E). No significant increase in aggregate area was observed for appl > NP-htt animals over the 50 days investigated (Fig. D, One-way ANOVA, $F = 1795$, $P < 0.0001$). Interestingly, the size of aggregates in appl > P-htt wings did not show an increase between days 5 and 10, however, a steady and gradual significant increase in the size of aggregates was observed in subsequent time points (Fig. 9 D). Significant differences in aggregate

Author Manuscript Author Manuscript Author Manuscript Author Manuscript

area were observed between the two genotypes after day 20, revealing significantly larger aggregates in the pathogenic version of htt (Fig. 9 D). The fluorescence intensity of appl > NP-htt wing aggregates did not show any significant increases, with one exception at day 20, where a large spike in fluorescence intensity was observed (Fig. 9 E, One-Way ANOVA, $F = 190.6$, $P < 0.0001$). Contrary to aggregate size, wing aggregates from appl > P-htt animals showed a steady increase in intensity from days 5-to-20, following by a dramatic decrease (Fig. 9 E). Significant differences in fluorescence intensity were observed between the two genotypes for the first 3 time-points (Fig. 9 E).

3.11. Neuronal expression of P-htt in adults shows significant reduction in lifespan

To assess the impacts of NP- and P-htt expression in the CNS of adult flies, initially a lifespan assay was conducted, again using Elav-Gal4. For the 3 control lines, the average lifespan of the 200 flies assessed for each genotype was over 80 days (Fig. 10 A, NP-htt, P-htt, Elav-Gal4). Flies expressing Elav > NP-htt did not show any reduction in lifespan compared to controls; 50 % lethality was 58 days in Elav > NP-htt flies compared to 66.0, 78.1, and 64.7 days in Elav, P-htt and NP-htt flies respectively. 90 % lethality at 75.3 days in Elav > NP-htt flies compared to 81.2, 98.4, and 95.5 for Elav, P-htt and NP-htt flies respectively (Fig. 10 A). However, Elav > P-htt expressing flies showed a drastically reduced lifespan compared to the other four genotypes, with 50 % lethality at 23.7 days, and 90 % lethality at 28.6 days (Fig. 10 A). These results are consistent with previous reports that expression of pathogenic human htt constructs in the NS of adult flies significantly reduces lifespan (Weiss et al., 2012).

3.12. Effects of htt expression on lifespan can be rescued by oral administration of the mTOR inhibitor rapamycin

Targeting the mTOR pathway has been shown to rescue lifespan deficits linked to polyQ disorders (The Huntington's Disease Collaborative Research Group, 1993; Kremer et al., 1994; Walker, 2007). Herein, we fed adult flies the mTOR inhibitor, rapamycin, to upregulate the mTOR dependent autophagy pathway, beginning either 8 or 15 days post-eclosion (Fig. 10 B, ref). Administration of rapamycin (200 μM rapamycin in standard food) 8- and 15-days post eclosion to adult Elav > P-htt flies dramatically rescued their lifespan: 50 % lethality at 26 and 31.6 days, and 90 % viability at 62.4 and 57.5 days, beginning feeding at 8 and 15-days post-eclosion respectively (Fig. 10 C). Supplementing our standard media with 200uM Rapamycin was able to more than double that lifespan of Elav > P-htt flies.

4. Discussion

Modeling Huntington's Disease in *Drosophila* facilitates a robust exploration of the molecular, cellular, physiological, and behavioral impacts of the disease. Remarkable genetic conservation exists between the fly and humans. Roughly 60 % of the 13,000 protein coding *Drosophila* genes are evolutionarily conserved in humans, and nearly 70 % of disease-causing genes in humans have fly orthologues (Reiter et al., 2001). Conducting sophisticated genetic manipulations in *Drosophila* is straight-forward and streamlined, and, given the size and collaborative-nature of the fly community, many mutant and transgenic

Author Manuscript Author Manuscript Author Manuscript Author Manuscript

lines are readily available (e.x. BDSC, VDRC, Kyoto). Numerous fundamental and basic pathways were discovered in the fly (circadian rhythm and notch) and *Drosophila* studies have contributed greatly to elucidating mechanisms of human neurodegenerative diseases (ex. Alzheimer's, Parkinson's, HD) (Greenspan and Dierick, 2004; Megaly et al., 2024). Consequently, rapid identification of therapeutic targets positions the model as a pivotal and unique tool in exploring the genetic implications of neurodegenerative diseases like HD. Herein we exploited many of these *Drosophila* attributes along with the powerful genetic and molecular toolkits, to enable precise *in vivo* tracking of HD development, progression and impacts on a wide range of cellular and gross structures. *In vivo* imaging facilitated tracking of the size, number, and fluorescence intensity of htt-aggregates as a function of time across precise windows of development. Animals with pathogenic htt exhibited aggregates of significantly greater number, size, and intensity at nearly all developmental time points. These aggregates caused severe trafficking impairments for organelles, up- and downstream of aggregates. While no obvious downstream effects were observed on the morphology of pre- and postsynaptic structures in the NMJ, or electrophysiological recordings, a distinct reduction in muscle force production was observed despite normal muscle ultrastructure. In our model of HD, animals expressing pathogenic htt exhibit locomotor deficits in both crawling velocity and distance. To longitudinally study HD in adult *Drosophila*, we developed a novel model for htt-aggregation in adult wings, which demonstrated similar patterns of htt-aggregate development to larvae. Lastly, pathogenic expression in the NS of flies results in significantly reduced viability, though supplementation of rapamycin, an mTOR pathway inhibitor, partially rescued fly viability and extended their lifespan.

A neuropathological hallmark of human HD is intracellular aggregation of N-terminal htt fragments, suggesting HD neuropathology is mediated by aberrant proteolytic cleavage or removal of htt fragments (Kim et al., 2001). While numerous proteases have been demonstrated to cleave N-terminal htt, proteolysis at the caspase-6 site is an important pathogenic event in HD (Wellington et al., 1998; Lunkes et al., 2002). *In vitro* expansion of N-terminal htt fragments enhances cytotoxicity, but site-directed mutagenesis of the caspase-6 cleavage site of N-terminal htt reduces cytotoxicity, suggesting inhibition of caspase cleavage of htt may be neuroprotective (Hackam et al., 1998; Wellington et al., 2000). Caspase-6 mediated N-terminal fragments of human htt were found to form aggregates throughout the soma, axons, and occasionally synapses of motor neurons (Akbergenova et al., 2018). In mouse models of HD, htt fragments formed aggregates progressively over time in the CNS, mirroring observations made in neuropathological studies of asymptomatic striatal, cerebral, and cerebellar brain slices from human HD patients (Sharp et al., 1995; Landles et al., 2010; Gutekunst et al., 1999a; Tagawa et al., 2004; Lunkes et al., 2002). In our study using a *Drosophila* model of HD, noticeable aggregates began forming in the somas in less than 24 HAH and continued to accumulate significantly until plateauing at 72 HAH. Similar effects were observed in the axons, increasing steadily from 48 to 96 HAH, then plateauing. The dynamics of htt-aggregate formation have been studied, both *in vitro* and *in vivo* models of HD, revealing similar patterns of mobility, proliferation, and accumulation (Weiss et al., 2012; Li et al., 2016). *In vitro* studies expressing fluorescently tagged exon 1 mhtt-94Q fragments

Author Manuscript Author Manuscript Author Manuscript Author Manuscript

in mouse embryonic stem cells have identified fast diffusion, dynamic clustering, and stable aggregation as three distinct dynamic states (Li et al., 2016). Single-molecule, super-resolution fluorescence imaging has tracked *htt* exon 1 with expanded polyQ aggregates from 80 nm globular species to 1 μm fibers, which further aggregate together into assemblies of increasing size (Duim et al., 2014). Sahl, et al. (2012) also visualized the formation of fibular aggregates ~100 nm in diameter and 1–2 μm in length in PC12 cells expressing exon 1 with an expanded polyQ region using fluorescence recovery after photobleaching (FRAP) to greatly enhance magnification and resolution of imaging (Sahl et al., 2012). *Drosophila* studies expressing fluorescently tagged exon 1 htt-138Q fragments identified rapid diffusion of fragments in axons, but faster incorporation of mobile htt-Q138 following aggregate formation and hasty reformation following FRAP (Weiss et al., 2012). *Drosophila* larvae expressing fluorescently tagged expanded polyQ exon 1 *htt* showed that large aggregates were immobile over a 2-h imaging period, and photobleached aggregates continue to add new *htt*, with nearly 50 % recover of the original fluorescence within an hour (Weiss et al., 2012). To enhance the imaging resolution to visualize the formation of individual *htt* fibers within aggregates may not be possible using this *in vivo* system, however this limitation will likely be overcome with ongoing technical and microscopy innovation. Nevertheless, our results also support these observations showing that initially fragmented P-htt accumulates into numerous, small aggregates, which increase in size exponentially over a few days, eventually reaching a plateau. Additionally, we demonstrated that SV and DCVs colocalized with htt-aggregates, suggesting that not only do htt-aggregates quickly accumulate new htt protein, but also act as an indiscriminate protein sink on a seconds-to-minutes timescale. Taken together, preventing, limiting, and clearing htt fragment aggregation could be a critical aspect of HD neuropathology and a target for treatment strategies.

Htt is a large ~350 KDa protein that undergoes a series of cleavages mediated through caspases, calpains, and aspartyl endopeptidases creating several naturally occurring fragmented products of the protein. While the length of polyQ region varies between investigation and research group, many experimental constructs employ full length or htt fragments containing 90+ glutamine repeats. In *Drosophila* 548 and 588 amino acid constructs revealed a clear aggregation phenotype that disrupted regular cell functions such as axonal trafficking and indiscriminate protein entrapment (Babcock and Ganetzky, 2015; Apostol et al., 2003; Lee et al., 2004). However no clear signs of toxicity or neurodegeneration are apparent in fragmented compared to the full length constructs (Romero et al., 2008). In mouse models, where a pathogenic human HTT exon 1 knock-ins replaced the mouse *htt* exon 1, distinct microaggregate bodies are observed in cortical tissue, along with progressive behavior and motor deficits, akin to crawling impairments observed herein (Sawada et al., 2007; Menalled et al., 2002). Other mice models expressing truncated 171 amino acid htt fragments show accumulation of cortical aggregates, while full-length *htt* displayed preferential striatal neurodegeneration as observed in humans (Yu et al., 2003; Gutekunst et al., 1999b; Kuemmerle et al., 1999b). Studies using *in vitro* models also show similar aggregation patterns to the vertebrate and invertebrate models above. Full length *htt* appears to be soluble and diffuse in the cytoplasm whereas truncated 63 and 171 amino acid htt fragments are typically insoluble aggregates (Cooper et al., 1998). Notably, short-stop exon 1 constructs in vertebrate, invertebrate and cell culture models

Author Manuscript Author Manuscript Author Manuscript Author Manuscript

appear to exhibit the greatest degree of aggregation, suggestive again that aberrant cleavage of expanded polyQ htt proteins is a prominent mediator of HD disease pathophysiology (Smith et al., 2023; Neueder et al., 2017; Ghosh et al., 2020; Yang et al., 2020; Graham et al., 2006b). Importantly, in most vertebrate and invertebrate models using full length *htt*, the cytoplasmically soluble protein does not tend to aggregate, but does exert hallmark neurodegenerative impacts. Taken together, reports in the field present strong evidence for truncated pathogenic htt causing cellular dysfunction while full length htt appears more cytotoxic. Still, it remains unclear if the different truncations exert distinct adverse effects or simply form aggregates that physically obstruct the dynamic and motile environment of the cell.

The endogenous, biological role of human htt remains unclear but previous studies have implicated htt in numerous processes including: as a scaffold protein, transcription regulation, neurogenesis, macroautophagy, cargo transport, and synaptic assembly and plasticity (Ochaba et al., 2014; Malla et al., 2021; Dragatsis et al., 2000; Martin et al., 2015; Caviston et al., 2007; Milnerwood and Raymond, 2010; Barron et al., 2022). These numerous roles are unsurprising given the large number of protein-protein interaction domains within htt, as well as its documented interactions with hundreds of proteins (Kaltenbach et al., 2007; Tourette et al., 2014). Furthermore, the subcellular localization of htt is fluid and dynamic, potentially due to an intrinsic capacity for intracellular compartment-dependent conformational changes (Ko et al., 2001). Antibodies recognizing different epitopes within htt reveal unique subcellular labelling including the nucleus, endosomes, ER, Golgi, axons, and synapses (Van Raamsdonk et al., 2005; Didiot et al., 2018; Gutekunst et al., 1995; Caviston et al., 2011; Leitman et al., 2013; del Toro et al., 2009; Li et al., 2003). Electron microscopy of htt reveals strong interactions between SVs and microtubules (Riguet et al., 2021). Here we demonstrate profound impacts of htt-aggregates on axonal trafficking of organelles. Both neurotransmitter-containing SVs and neuropeptide-containing DCVs are trafficked along the axonal microtubules *via* canonical molecular motor machinery (Lim et al., 2017; Okada et al., 1995) While a direct interaction between dynein/dynactin has been identified, htt is known to be a critical scaffold for both molecular motors: kinesin and the dynein/dynactin complex (Caviston et al., 2007; Caviston et al., 2011; McGuire et al., 2006). Huntington-associated-protein-1 (HAP1), one of the earliest identified binding partners of htt, directly binds to Kinesin-light-chain (KLC) and Dynactin $p150^{glued}$, as evidenced by mutations or alterations in HAP1 expression are known to significantly impair axonal trafficking dynamics. Pathogenic htt has been demonstrated to exhibit a higher binding affinity for HAP1, leading to breakdowns in the intracellular trafficking of SVs, DCVs, and mitochondria (McGuire et al., 2006; Engelender et al., 1997; Li et al., 1998). Furthermore, a critical stretch of 17 amino-acids at the start of N-terminal of htt regulates mitochondrial and ER localization (Rockabrand et al., 2007). Htt is also known to facilitate clathrin-mediated vesicle trafficking into endosomes *via* its interaction with Huntingtin-interacting protein 1 (HIP1) (Liu et al., 2023). In dendrites, htt has been found directly interacting with dynein to mediate trafficking of TrkB-containing vesicles, representing a more extensive transport role for htt (Liot et al., 2013). We investigated organelle trafficking both up- and downstream of aggregates to distinguish the endogenous role of htt in trafficking organelles from the effect of aggregates on downstream trafficking.

Author Manuscript Author Manuscript Author Manuscript Author Manuscript

Trafficking of SVs and DCVs was significantly impaired upstream of htt-aggregates, supporting the critical role of htt in regulating molecular trafficking. Interestingly, an even greater impact of P-htt was observed on trafficking downstream of aggregates, suggesting the effects of aggregation outweigh the defects in its role in supporting molecular transport proteins. Aggregation not only impairs trafficking by acting as a sink for newly trafficking htt, but it severely limits downstream trafficking of organelles. Collectively, these results suggest expansion of the polyQ region in exon 1 of htt alters the endogenous functionality of the protein, its association with other critical motor proteins, and leads to aggregation that severely impairs organelle trafficking, among other cellular functions.

Vesicular transport deficits in BDNF are known to play a critical role in HD (Szebenyi et al., 2003; Gunawardena et al., 2003). Consequently, we explored the impacts of P-htt on the trafficking dynamics of BDNF and found a dramatic reduction in its molecular transport. Studies have shown that decreasing BDNF production in cortical neurons results in degeneration of the striatum, but restoring BDNF secretion promotes neuronal survival (Ivkovic and Ehrlich, 1999; Rauskolb et al., 2010; Bosse et al., 2012). While BDNF is not directly produced in striatal neurons, it is transported to the striatum by corticostriatial-projecting neurons in the cortex (Altar et al., 1997). Although several models of HD pathology implicate pathogenic htt-mediated trafficking deficits in late-onset symptoms, numerous other adult-onset neurodegenerative disease are attributed to transport breakdowns, indicating a strong link between trafficking deficits and neurodegeneration pathology generally (Perlson et al., 2010).

Surprisingly, htt aggregation and trafficking deficits observed herein did not alter the morphology or electrophysiological properties of the neuromuscular junction. As such, evidence of neuronal degeneration downstream of numerous, large htt aggregates was not overt. Presynaptic motor neurons formed seemingly wild-type innervation along the surface of body wall muscles. At the ultrastructural level, no changes in bouton number or AZ density were observed in either glutamatergic motor neuron subtypes. Similarly, postsynaptic muscle fibers were structurally normal at both gross and ultrastructural organizational levels. It is important to note the presence of satellite boutons, indicative of a putative compensatory mechanism deployed by the neuron to mitigate transmission deficits, consistent with previous reports (Akbergenova and Littleton, 2017). Indeed, insoluble aggregates formed in the axoplasm do not lead to neurodegeneration, but evidence suggests that nuclear aggregates could contribute to the neurodegenerative processes (Gutekunst et al., 1999a; Kuemmerle et al., 1999a; Cha et al., 1998). Nuclear aggregates have been shown to sequester cAMP response element-binding protein (CREB), a critical transcription factor for mediating cell survival, contributing significantly to neurodegeneration observed in HD and other neurological disorders (Jiang et al., 2006). Studies have demonstrated that soluble forms of polyQ-htt, rather than insoluble aggregates, contribute to neurodegeneration despite the severe reductions in lifespan observed when large aggregates are expressed in the NS (Weiss et al., 2012; Arrasate et al., 2004). Indeed, studies in mice show neurodegeneration in the absence of htt-aggregation (Kuemmerle et al., 1999a; Hodgson et al., 1999; Slow et al., 2003). Furthermore, despite striatal neurons being the site of highest degree of neurodegeneration in human patients, aggregates observed in these neurons are exceedingly rare (Gutekunst et al., 1999a). While multiple studies have demonstrated that

Author Manuscript Author Manuscript Author Manuscript Author Manuscript

nuclear translocation of htt increases cytotoxicity and neuropathy, evidence also shows widespread nuclear htt without exhibiting neurotoxicity (Hoffner et al., 2007; Zheng et al., 2013). It is therefore difficult to determine whether expanded polyQ N-terminal fragments of htt are sufficient for disease progression, or if another fragment of htt is needed for nuclear localization and/or neurodegeneration. Nevertheless, while no obvious effects were observed to support either developmental perturbation or expanded polyQ htt fragment aggregate-induced changes in NMJ morphology, profound effects on muscle contractility were observed.

One of the earliest clinically diagnosed symptoms of HD is chorea, involuntary jerking or writhing movements typically associated with altered CNS functionality (Schiefer et al., 2015). However, recent work has focused on the effects of HD in peripheral tissues, including muscles (Corrochano et al., 2018; Bozzi and Sciandra, 2020). Using a microforce transducer system, we observed significantly reduced muscle contraction force in animals expressing the expanded polyQ htt fragment. Muscle force production was most severely impaired during 10–50 Hz motor neuron stimulation, previously identified as the most plastic and modifiable stimulation frequency (Ormerod et al., 2022). Descending motor output recorded from intact larvae show stimulation frequencies ranging from 1 to 150 Hz, while fictive muscle contraction recordings demonstrated 25–30 Hz as the most common during rhythmic peristalsis (Ormerod et al., 2022). Shorter duration stimulation bursts (200–300 ms) were more severely impacted, but significant effects were observed during pronounced 900 ms duration stimulations. The rise and decay time kinetics were also severely impacted, indicating potential issues with calcium liberation, or other aspects of the excitation-contraction coupling machinery (Ormerod et al., 2022). Given these well-defined descending output frequencies underlying muscle contraction and locomotion, it is not surprising low-frequency stimulation EJPs did not reveal a significant change. High frequency stimulation underlying locomotion triggers many well-characterized dynamic processes at the bouton (Akbergenova and Bykhovskaia, 2009; Vasin et al., 2014; Goel and Dickman, 2021). High frequency dependent cycling of the readily releasable, recycling, and reserve pools and new supplies of synaptic materials from the soma are tightly regulated processes critical for normal muscle functionality (Guan et al., 2020). Furthermore, the presence of aggregates in motor neurons at critical branching points observed herein may cause AP failure during high frequency stimulation (Baccus et al., 2000). Thus, the molecular machinery and metabolic demand during fictive contraction recordings is likely a better representation of the downstream impacts of htt-fragment aggregates on neuromuscular transduction. However, more robust electrophysiological explorations would provide insight into how htt-aggregates affect behavior. To address this limitation, subsequent works should explore high frequency stimulation paradigms and CPG recordings to potentially elucidate the link between muscle development and muscle performance. Given that atrophy and skeletal muscle wasting is a common hallmark of HD, it is not surprising that transcriptional changes in skeletal tissues were comparable to those observed in different brain regions (Bozzi and Sciandra, 2020). Several mechanisms have been implicated in skeletal muscle HD pathology, including mitochondrial abnormalities, cytotoxic aggregation, and reduced heat shock transcription factor 1 (Neueder et al., 2024; Romer et al., 2021; Kim and Gomez-Pastor, 2023; Gomez-Pastor et al., 2018). However,

Author Manuscript Author Manuscript Author Manuscript Author Manuscript

the impacts of HD on neuromuscular transmission and muscle physiology remain poorly investigated (Gomez-Pastor et al., 2018). Importantly, improving muscle function in murine models delays HD onset and improves life-span (Caldwell et al., 2020), and exercise in humans has been shown to improve countless metrics of skeletal muscle pathophysiology in HD patients (Deligiannis et al., 2021). Taken together, investigations of HD on skeletal muscles, and targeting skeletal muscle for therapies are important future directions.

Treatments targeting aggregation centered around protein stabilization, administration of small molecule inhibitors, and upregulating cell-clearance mechanisms show promising improvements in aggregate reduction and mitigating functional deficits. (Carmichael et al., 2000; Chopra et al., 2007; Sarkar et al., 2009a) Considerable research has implicated a strong link between HD and altered macroautophagy, highlighted by a severe reduction in neuronal capacity to degrade misfolded proteins (Pircs et al., 2022). Given that P-htt misfolds and forms insoluble aggregates, targeting autophagy was of particular interest in our current investigation. P-htt has been shown to alter cellular levels of Argonaute 2, a critical protein of the RISC complex modulating post transcriptional regulation of gene expression, caused by reduced autophagy leading to both neurodegeneration and functional deficits (Pircs et al., 2018). Furthermore, P-htt has been shown to sequester autophagosomes, further emphasizing htt-aggregates as sink (Rui et al., 2015). Rapamycin, a macrolide mTOR inhibitor, has been demonstrated to both delay and rescue neuronal dysfunction in models of HD (Saliba et al., 2017; Sarkar et al., 2009b; Roth et al., 2023). Rapamycin treatment upregulates Atg1 which is critical in the recruitment of other Atg proteins responsible for autophagosome synthesis (Mizushima, 2010; Stjepanovic et al., 2014). Additionally, inhibition of TORC1 by rapamycin depresses protein synthesis in the cell and leads to activation of ULK1 (Atg1 homolog), an integral component of autophagosome formation (Lamming, 2016). Unsurprisingly, administration of rapamycin has been shown to enhance P-htt clearance leading to rescue of locomotor function of *Drosophila (*Roth et al., 2023). Previous studies have shown rapamycin to have antiproliferative properties, associated with an effect on lifespan and viability (Lee et al., 2024; Bjedov et al., 2010). We explored the effect of these properties by supplementing the food of adult *Drosophila* expressing P-htt with 200 uM rapamycin, which resulted in an effective doubling of their lifespan. Compiling all the evidence, exploration of htt aggregation on disrupting the RNA silencing and autophagy machineries may provide a key link to delaying or preventing aggregate proliferation on cellular fate.

HD remains a challenging disorder to study due to the complex role of the htt protein in various cellular processes. In this study, we reveal the role of P-htt in disrupting the molecular motor machinery and its tendency to form aggregates that indiscriminately trap axonal cargo. Additionally, we observe significant deficits in muscle contractility and locomotory behavior reminiscent of chorea, despite no noticeable deformities in NMJ formation or muscle ultrastructure. Targeted therapies, whether pharmacological or genetic, will depend on a comprehensive understanding of the pathophysiological effects of P-htt aggregates and their downstream targets, which may extend beyond the nervous system.

Future investigations could expand upon the findings herein or expand upon the technical limitations the relationship between aggregate size and trafficking deficits, and observe

Author Manuscript Author Manuscript Author Manuscript Author Manuscript

precise aggregation temporal dynamics both within individual neurons, and different neuronal subtypes.

Acknowledgements

Research supported by the National Institute of General Medical Sciences of the National Institutes of Health under Award Number R15GM155985 to KGO. Generous financial support from Middle Tennessee State University to KGO. The authors would like to thank Professor Troy Littleton for generously providing the UAS-NP-htt (mRFP-HttQ15), UAS-P-htt (mRFP-HttQ138), and UAS-Syt1-GFP constructs, as well as the GluRIII antibody. We would also like to thank Dr. Yulia Akbergenova for her insights on the manuscript.

Data availability

Data will be made available on request.

References

Akbergenova Y, Bykhovskaia M, 2009. Stimulation-induced formation of the reserve pool of vesicles in Drosophila motor boutons. J. Neurophysiol 101, 2423–2433. 10.1152/jn.91122.2008. [PubMed: 19279147]

Akbergenova Y, Littleton JT, 2017. Pathogenic Huntington alters BMP signaling and synaptic growth through local disruptions of endosomal compartments. J. Neurosci 37, 3425–3439. 10.1523/JNEUROSCI.2752-16.2017. [PubMed: 28235896]

Akbergenova Y, Cunningham KL, Zhang YV, Weiss S, Littleton JT, 2018. Characterization of developmental and molecular factors underlying release heterogeneity at Drosophila synapses. eLife 7. 10.7554/eLife.38268.

Altar CA, Cai N, Bliven T, Juhasz M, Conner JM, Acheson AL, Lindsay RM, Wiegand SJ, 1997. Anterograde transport of brain-derived neurotrophic factor and its role in the brain. Nature 389, 856–860. 10.1038/39885. [PubMed: 9349818]

Aponte-Santiago NA, Ormerod KG, Akbergenova Y, Littleton JT, 2020. Synaptic plasticity induced by differential manipulation of tonic and phasic motoneurons in drosophila. J. Neurosci 40, 6270–6288. 10.1523/JNEUROSCI.0925-20.2020. [PubMed: 32631939]

Apostol BL, Kazantsev A, Raffioni S, Illes K, Pallos J, Bodai L, Slepko N, Bear JE, Gertler FB, Hersch S, et al. , 2003. A cell-based assay for aggregation inhibitors as therapeutics of polyglutamine-repeat disease and validation in Drosophila. Proc. Natl. Acad. Sci. USA 100, 5950–5955. 10.1073/pnas.2628045100. [PubMed: 12730384]

Arrasate M, Mitra S, Schweitzer ES, Segal MR, Finkbeiner S, 2004. Inclusion body formation reduces levels of mutant huntingtin and the risk of neuronal death. Nature 431, 805–810. 10.1038/nature02998. [PubMed: 15483602]

Babcock DT, Ganetzky B, 2015. Transcellular spreading of huntingtin aggregates in the Drosophila brain. Proc. Natl. Acad. Sci. USA 112, E5427–E5433. 10.1073/pnas.1516217112. [PubMed: 26351672]

Baccus SA, Burrell BD, Sahley CL, Muller KJ, 2000. Action potential reflection and failure at axon branch points cause stepwise changes in EPSPs in a neuron essential for learning. J. Neurophysiol 83, 1693–1700. 10.1152/jn.2000.83.3.1693. [PubMed: 10712489]

Barron JC, Nafar F, Parsons MP, 2022. Huntingtin is essential for synaptic plasticity in the adult hippocampus. BioRxiv. 10.1101/2022.10.05.510980.

Bates GP, Dorsey R, Gusella JF, Hayden MR, Kay C, Leavitt BR, Nance M, Ross CA, Scahill RI, Wetzel R, et al. , 2015. Huntington disease. Nat. Rev. Dis. Primers 1, 15005. 10.1038/nrdp.2015.5. [PubMed: 27188817]

Bjedov I, Toivonen JM, Kerr F, Slack C, Jacobson J, Foley A, Partridge L, 2010. Mechanisms of life span extension by rapamycin in the fruit fly Drosophila melanogaster. Cell Metab. 11, 35–46. 10.1016/j.cmet.2009.11.010. [PubMed: 20074526]

Author Manuscript Author Manuscript Author Manuscript Author Manuscript

Bosse KE, Maina FK, Birbeck JA, France MM, Roberts JJP, Colombo ML, Mathews TA, 2012. Aberrant striatal dopamine transmitter dynamics in brain-derived neurotrophic factor-deficient mice. J. Neurochem 120, 385–395. 10.1111/j.1471-4159.2011.07531.x. [PubMed: 21988371]

Bozzi M, Sciandra F, 2020. Molecular mechanisms underlying muscle wasting in huntington's disease. Int. J. Mol. Sci 21. 10.3390/ijms21218314.

Branson K, Robie AA, Bender J, Perona P, Dickinson MH, 2009. High-throughput ethomics in large groups of Drosophila. Nat. Methods 6, 451–457. 10.1038/nmeth.1328. [PubMed: 19412169]

Caldwell CC, Petzinger GM, Jakowec MW, Cadenas E, 2020. Treadmill exercise rescues mitochondrial function and motor behavior in the CAG140 knock-in mouse model of Huntington's disease. Chem. Biol. Interact 315, 108907. 10.1016/j.cbi.2019.108907.

Carmichael J, Chatellier J, Woolfson A, Milstein C, Fersht AR, Rubinsztein DC, 2000. Bacterial and yeast chaperones reduce both aggregate formation and cell death in mammalian cell models of Huntington's disease. Proc. Natl. Acad. Sci. USA 97, 9701–9705. 10.1073/pnas.170280697. [PubMed: 10920207]

Caviston JP, Ross JL, Antony SM, Tokito M, Holzbaur ELF, 2007. Huntingtin facilitates dynein/dynactin-mediated vesicle transport. Proc. Natl. Acad. Sci. USA 104, 10045–10050. 10.1073/pnas.0610628104. [PubMed: 17548833]

Caviston JP, Zajac AL, Tokito M, Holzbaur ELF, 2011. Huntingtin coordinates the dynein-mediated dynamic positioning of endosomes and lysosomes. Mol. Biol. Cell 22, 478–492. 10.1091/mbc.E10-03-0233. [PubMed: 21169558]

Cha JH, Kosinski CM, Kerner JA, Alsdorf SA, Mangiarini L, Davies SW, Penney JB, Bates GP, Young AB, 1998. Altered brain neurotransmitter receptors in transgenic mice expressing a portion of an abnormal human Huntington disease gene. Proc. Natl. Acad. Sci. USA 95, 6480–6485. 10.1073/pnas.95.11.6480. [PubMed: 9600992]

Chang DTW, Rintoul GL, Pandipati S, Reynolds IJ, 2006. Mutant huntingtin aggregates impair mitochondrial movement and trafficking in cortical neurons. Neurobiol. Dis 22, 388–400. 10.1016/j.nbd.2005.12.007. [PubMed: 16473015]

Chen X, He E, Su C, Zeng Y, Xu J, 2023. Huntingtin-associated protein 1-associated intracellular trafficking in neurodegenerative diseases. Front. Aging Neurosci. 15, 1100395. 10.3389/fnagi.2023.1100395.

Chopra V, Fox JH, Lieberman G, Dorsey K, Matson W, Waldmeier P, Housman DE, Kazantsev A, Young AB, Hersch S, 2007. A small-molecule therapeutic lead for Huntington's disease: preclinical pharmacology and efficacy of C2–8 in the R6/2 transgenic mouse. Proc. Natl. Acad. Sci. USA 104, 16685–16689. 10.1073/pnas.0707842104. [PubMed: 17925440]

Cohen-Carmon D, Meshorer E, 2012. Polyglutamine (polyQ) disorders: the chromatin connection. Nucleus 3, 433–441. 10.4161/nucl.21481. [PubMed: 22892726]

Cooper JK, Schilling G, Peters MF, Herring WJ, Sharp AH, Kaminsky Z, Masone J, Khan FA, Delanoy M, Borchelt DR, et al. , 1998. Truncated N-terminal fragments of huntingtin with expanded glutamine repeats form nuclear and cytoplasmic aggregates in cell culture. Hum. Mol. Genet 7, 783–790. 10.1093/hmg/7.5.783. [PubMed: 9536081]

Corrochano S, Blanco G, Acevedo-Arozena A, 2018. Skeletal muscle modulates huntington's disease pathogenesis in mice: role of physical exercise. J. Exp. Neurosci 12. 10.1177/1179069518809059, 1179069518809059.

Cox RT, Spradling AC, 2003. A Balbiani body and the fusome mediate mitochondrial inheritance during Drosophila oogenesis. Development 130, 1579–1590. 10.1242/dev.00365. [PubMed: 12620983]

Cunningham KL, Littleton JT, 2022. Mechanisms controlling the trafficking, localization, and abundance of presynaptic Ca2+ channels. Front. Mol. Neurosci 15, 1116729. 10.3389/fnmol.2022.1116729.

del Toro D, Alberch J, Lázaro-Diéguez F, Martín-Ibáñez R, Xifró X, Egea G, Canals JM, 2009. Mutant huntingtin impairs post-Golgi trafficking to lysosomes by delocalizing optineurin/Rab8 complex from the Golgi apparatus. Mol. Biol. Cell 20, 1478–1492. 10.1091/mbc.e08-07-0726. [PubMed: 19144827]

Author Manuscript Author Manuscript Author Manuscript Author Manuscript

Deligiannis A, D'Alessandro C, Cupisti A, 2021. Exercise training in dialysis patients: impact on cardiovascular and skeletal muscle health. Clin. Kidney J 14. 10.1093/ckj/sfaa273 ii25–ii33.

Didiot M-C, Ferguson CM, Ly S, Coles AH, Smith AO, Bicknell AA, Hall LM, Sapp E, Echeverria D, Pai AA, et al. , 2018. Nuclear localization of huntingtin mRNA is specific to cells of neuronal origin. Cell Rep. 24, 2553–2560.e5. 10.1016/j.celrep.2018.07.106. [PubMed: 30184490]

Dragatsis I, Levine MS, Zeitlin S, 2000. Inactivation of Hdh in the brain and testis results in progressive neurodegeneration and sterility in mice. Nat. Genet 26, 300–306. 10.1038/81593. [PubMed: 11062468]

Duim WC, Jiang Y, Shen K, Frydman J, Moerner WE, 2014. Super-resolution fluorescence of huntingtin reveals growth of globular species into short fibers and coexistence of distinct aggregrates. ACS Chem. Biol 9, 2767–2778. [PubMed: 25330023]

Engelender S, Sharp AH, Colomer V, Tokito MK, Lanahan A, Worley P, Holzbaur EL, Ross CA, 1997. Huntingtin-associated protein 1 (HAP1) interacts with the p150Glued subunit of dynactin. Hum. Mol. Genet 6, 2205–2212. 10.1093/hmg/6.13.2205. [PubMed: 9361024]

Fan H-C, Ho L-I, Chi C-S, Chen S-J, Peng G-S, Chan T-M, Lin S-Z, Harn H-J, 2014. Polyglutamine (PolyQ) diseases: genetics to treatments. Cell Transplant. 23, 441–458. 10.3727/096368914X678454. [PubMed: 24816443]

Fang Y, Soares L, Bonini NM, 2013. Design and implementation of in vivo imaging of neural injury responses in the adult Drosophila wing. Nat. Protoc 8, 810–819. 10.1038/nprot.2013.042. [PubMed: 23589940]

Feng Y, Ueda A, Wu C-F, 2004. A modified minimal hemolymph-like solution, HL3.1, for physiological recordings at the neuromuscular junctions of normal and mutant Drosophila larvae. J. Neurogenet 18, 377–402. 10.1080/01677060490894522. [PubMed: 15763995]

Gauthier LR, Charrin BC, Borrell-Pagès M, Dompierre JP, Rangone H, Cordelières FP, De Mey J, MacDonald ME, Lessmann V, Humbert S, et al. , 2004. Huntingtin controls neurotrophic support and survival of neurons by enhancing BDNF vesicular transport along microtubules. Cell 118, 127–138. 10.1016/j.cell.2004.06.018. [PubMed: 15242649]

Ghosh R, Wood-Kaczmar A, Dobson L, Smith EJ, Sirinathsinghji EC, Kriston-Vizi J, Hargreaves IP, Heaton R, Herrmann F, Abramov AY, et al. , 2020. Expression of mutant exon 1 huntingtin fragments in human neural stem cells and neurons causes inclusion formation and mitochondrial dysfunction. FASEB J. 34, 8139–8154. 10.1096/fj.201902277RR. [PubMed: 32329133]

Goel P, Dickman D, 2021. Synaptic homeostats: latent plasticity revealed at the Drosophila neuromuscular junction. Cell. Mol. Life Sci 78, 3159–3179. 10.1007/s00018-020-03732-3. [PubMed: 33449150]

Gomez-Pastor R, Burchfiel ET, Thiele DJ, 2018. Regulation of heat shock transcription factors and their roles in physiology and disease. Nat. Rev. Mol. Cell Biol. 19, 4–19. 10.1038/nrm.2017.73. [PubMed: 28852220]

Gondré-Lewis MC, Park JJ, Loh YP, 2012. Cellular mechanisms for the biogenesis and transport of synaptic and dense-core vesicles. Int. Rev. Cell Mol. Biol 299, 27–115. 10.1016/B978-0-12-394310-1.00002-3. [PubMed: 22959301]

Graham RK, Deng Y, Slow EJ, Haigh B, Bissada N, Lu G, Pearson J, Shehadeh J, Bertram L, Murphy Z, et al. , 2006a. Cleavage at the caspase-6 site is required for neuronal dysfunction and degeneration due to mutant huntingtin. Cell 125, 1179–1191. 10.1016/j.cell.2006.04.026. [PubMed: 16777606]

Graham RK, Deng Y, Slow EJ, Haigh B, Bissada N, Lu G, Pearson J, Shehadeh J, Bertram L, Murphy Z, et al. , 2006b. Cleavage at the caspase-6 site is required for neuronal dysfunction and degeneration due to mutant huntingtin. Cell 125, 1179–1191. 10.1016/j.cell.2006.04.026. [PubMed: 16777606]

Greenspan RJ, Dierick HA, 2004. Am not I a fly like thee?' From genes in fruit flies to behavior in humans. Hum. Mol. Genet 10.1093/hmg/ddh248.

Guan Z, Quiñones-Frías MC, Akbergenova Y, Littleton JT, 2020. Drosophila Synaptotagmin 7 negatively regulates synaptic vesicle release and replenishment in a dosage-dependent manner. eLife 9. 10.7554/eLife.55443.

Author Manuscript Author Manuscript Author Manuscript Author Manuscript

Gunawardena S, Her L-S, Brusch RG, Laymon RA, Niesman IR, Gordesky-Gold B, Sintasath L, Bonini NM, Goldstein LSB, 2003. Disruption of axonal transport by loss of huntingtin or expression of pathogenic polyQ proteins in Drosophila. Neuron 40, 25–40. 10.1016/s0896-6273(03)00594-4. [PubMed: 14527431]

Gutekunst CA, Levey AI, Heilman CJ, Whaley WL, Yi H, Nash NR, Rees HD, Madden JJ, Hersch SM, 1995. Identification and localization of huntingtin in brain and human lymphoblastoid cell lines with anti-fusion protein antibodies. Proc. Natl. Acad. Sci. USA 92, 8710–8714. 10.1073/pnas.92.19.8710. [PubMed: 7568002]

Gutekunst CA, Li SH, Yi H, Mulroy JS, Kuemmerle S, Jones R, Rye D, Ferrante RJ, Hersch SM, Li XJ, 1999a. Nuclear and neuropil aggregates in Huntington's disease: relationship to neuropathology. J. Neurosci 19, 2522–2534. 10.1523/JNEUROSCI.19-07-02522.1999. [PubMed: 10087066]

Gutekunst CA, Li SH, Yi H, Mulroy JS, Kuemmerle S, Jones R, Rye D, Ferrante RJ, Hersch SM, Li XJ, 1999b. Nuclear and neuropil aggregates in Huntington's disease: relationship to neuropathology. J. Neurosci 19, 2522–2534. 10.1523/JNEUROSCI.19-07-02522.1999. [PubMed: 10087066]

Hackam AS, Singaraja R, Wellington CL, Metzler M, McCutcheon K, Zhang T, Kalchman M, Hayden MR, 1998. The influence of huntingtin protein size on nuclear localization and cellular toxicity. J. Cell Biol. 141, 1097–1105. 10.1083/jcb.141.5.1097. [PubMed: 9606203]

Hodgson JG, Agopyan N, Gutekunst CA, Leavitt BR, LePiane F, Singaraja R, Smith DJ, Bissada N, McCutcheon K, Nasir J, et al. , 1999. A YAC mouse model for Huntington's disease with full-length mutant huntingtin, cytoplasmic toxicity, and selective striatal neurodegeneration. Neuron 23, 181–192. 10.1016/s0896-6273(00)80764-3. [PubMed: 10402204]

Hoffner G, Souès S, Djian P, 2007. Aggregation of expanded huntingtin in the brains of patients with Huntington disease. Prion 1, 26–31. [PubMed: 19172113]

Holmes SE, O'Hearn EE, McInnis MG, Gorelick-Feldman DA, Kleiderlein JJ, Callahan C, Kwak NG, Ingersoll-Ashworth RG, Sherr M, Sumner AJ, et al. , 1999. Expansion of a novel CAG trinucleotide repeat in the 5′ region of PPP2R2B is associated with SCA12. Nat. Genet 23, 391–392. 10.1038/70493. [PubMed: 10581021]

Hoskins RA, Phan AC, Naeemuddin M, Mapa FA, Ruddy DA, Ryan JJ, Young LM, Wells T, Kopczynski C, Ellis MC, 2001. Single nucleotide polymorphism markers for genetic mapping in Drosophila melanogaster. Genome Res. 11, 1100–1113. 10.1101/gr.gr-1780r. [PubMed: 11381036]

Hummer BH, de Leeuw NF, Burns C, Chen L, Joens MS, Hosford B, Fitzpatrick JAJ, Asensio CS, 2017. HID-1 controls formation of large dense core vesicles by influencing cargo sorting and trans-Golgi network acidification. Mol. Biol. Cell 28, 3870–3880. 10.1091/mbc.E17-08-0491. [PubMed: 29074564]

Ivkovic S, Ehrlich ME, 1999. Expression of the striatal DARPP-32/ARPP-21 phenotype in GABAergic neurons requires neurotrophins in vivo and in vitro. J. Neurosci 19, 5409–5419. 10.1523/JNEUROSCI.19-13-05409.1999. [PubMed: 10377350]

Jan LY, Jan YN, 1976. Properties of the larval neuromuscular junction in Drosophila melanogaster. J. Physiol. Lond 262, 189–214. 10.1113/jphysiol.1976.sp011592. [PubMed: 11339]

Jiang H, Poirier MA, Liang Y, Pei Z, Weiskittel CE, Smith WW, DeFranco DB, Ross CA, 2006. Depletion of CBP is directly linked with cellular toxicity caused by mutant huntingtin. Neurobiol. Dis 23, 543–551. 10.1016/j.nbd.2006.04.011. [PubMed: 16766198]

Juenemann K, Weisse C, Reichmann D, Kaether C, Calkhoven CF, Schilling G, 2011. Modulation of mutant huntingtin N-terminal cleavage and its effect on aggregation and cell death. Neurotox. Res 20, 120–133. 10.1007/s12640-010-9227-6. [PubMed: 21116768]

Kaltenbach LS, Romero E, Becklin RR, Chettier R, Bell R, Phansalkar A, Strand A, Torcassi C, Savage J, Hurlburt A, et al. , 2007. Huntingtin interacting proteins are genetic modifiers of neurodegeneration. PLoS Genet. 3, e82. 10.1371/journal.pgen.0030082. [PubMed: 17500595]

Kim H, Gomez-Pastor R, 2023. HSF1 and its role in huntington's disease pathology.Adv. Exp. Med. Biol 1410, 35–95. 10.1007/5584_2022_742. [PubMed: 36396925]

Kim YJ, Yi Y, Sapp E, Wang Y, Cuiffo B, Kegel KB, Qin ZH, Aronin N, DiFiglia M, 2001. Caspase 3-cleaved N-terminal fragments of wild-type and mutant huntingtin are present in normal

Author Manuscript Author Manuscript Author Manuscript Author Manuscript

and Huntington's disease brains, associate with membranes, and undergo calpain-dependent proteolysis. Proc. Natl. Acad. Sci. USA 98, 12784–12789. 10.1073/pnas.221451398. [PubMed: 11675509]

Ko J, Ou S, Patterson PH, 2001. New anti-huntingtin monoclonal antibodies: implications for huntingtin conformation and its binding proteins. Brain Res. Bull 56, 319–329. 10.1016/S0361-9230(01)00599-8. [PubMed: 11719267]

Kremer B, Goldberg P, Andrew SE, Theilmann J, Telenius H, Zeisler J, Squitieri F, Lin B, Bassett A, Almqvist E, 1994. A worldwide study of the Huntington's disease mutation. The sensitivity and specificity of measuring CAG repeats. N. Engl. J. Med 330, 1401–1406. 10.1056/NEJM199405193302001. [PubMed: 8159192]

Kuemmerle S, Gutekunst CA, Klein AM, Li XJ, Li SH, Beal MF, Hersch SM, Ferrante RJ, 1999a. Huntington aggregates may not predict neuronal death in Huntington's disease. Ann. Neurol 46, 842–849. [PubMed: 10589536]

Kuemmerle S, Gutekunst CA, Klein AM, Li XJ, Li SH, Beal MF, Hersch SM, Ferrante RJ, 1999b. Huntington aggregates may not predict neuronal death in Huntington's disease. Ann. Neurol 46, 842–849. [PubMed: 10589536]

Kuznetsov IA, Kuznetsov AV, 2017. How dense core vesicles are delivered to axon terminals – A review of modeling approaches. In: Modeling of Microscale Transport in Biological Processes. Elsevier, pp. 335–352. 10.1016/B978-0-12-804595-4.00013-4.

La Spada AR, Taylor JP, 2003. Polyglutamines placed into context. Neuron 38, 681–684. 10.1016/s0896-6273(03)00328-3. [PubMed: 12797953]

La Spada AR, Roling DB, Harding AE, Warner CL, Spiegel R, Hausmanowa-Petrusewicz I, Yee WC, Fischbeck KH, 1992. Meiotic stability and genotype-phenotype correlation of the trinucleotide repeat in X-linked spinal and bulbar muscular atrophy. Nat. Genet 2, 301–304. 10.1038/ng1292-301. [PubMed: 1303283]

Lamming DW, 2016. Inhibition of the mechanistic target of rapamycin (mTOR)-rapamycin and beyond. Cold Spring Harb. Perspect. Med 6. 10.1101/cshperspect.a025924.

Landles C, Sathasivam K, Weiss A, Woodman B, Moffitt H, Finkbeiner S, Sun B, Gafni J, Ellerby LM, Trottier Y, et al. , 2010. Proteolysis of mutant huntingtin produces an exon 1 fragment that accumulates as an aggregated protein in neuronal nuclei in Huntington disease. J. Biol. Chem 285, 8808–8823. 10.1074/jbc.M109.075028. [PubMed: 20086007]

Lee J, Littleton JT, 2015. Transmembrane tethering of synaptotagmin to synaptic vesicles controls multiple modes of neurotransmitter release. Proc. Natl. Acad. Sci. USA 112, 3793–3798. 10.1073/pnas.1420312112. [PubMed: 25775572]

Lee W-C, Yoshihara M, Littleton JT, 2004. Cytoplasmic aggregates trap polyglutamine containing porteins and block axonal transport in a Drosophila model of huntington's disease. PNAS 101 (9), 3224–3229. [PubMed: 14978262]

Lee DJW, Hodzic Kuerec A, Maier AB, 2024. Targeting ageing with rapamycin and its derivatives in humans: a systematic review. Lancet Healthy Longev. 5, e152–e162. 10.1016/S2666-7568(23)00258-1. [PubMed: 38310895]

Leitman J, Ulrich Hartl F, Lederkremer GZ, 2013. Soluble forms of polyQ-expanded huntingtin rather than large aggregates cause endoplasmic reticulum stress. Nat. Commun 4, 2753. 10.1038/ncomms3753. [PubMed: 24217578]

Li SH, Hosseini SH, Gutekunst CA, Hersch SM, Ferrante RJ, Li XJ, 1998. A human HAP1 homologue. Cloning, expression, and interaction with huntingtin. J. Biol. Chem 273, 19220–19227. 10.1074/jbc.273.30.19220. [PubMed: 9668110]

Li J-Y, Plomann M, Brundin P, 2003. Huntington's disease: a synaptopathy? Trends Mol. Med 9, 414–420. 10.1016/j.molmed.2003.08.006. [PubMed: 14557053]

Li L, Liu H, Dong P, Li D, Legant WR, Grimm JB, Lavis LD, Betzig E, Tjian R, Liu Z, 2016. Real-time imaging of Huntingtin aggregates diverting target search and gene transcription. eLife 5. 10.7554/eLife.17056.

Lim A, Rechtsteiner A, Saxton WM, 2017. Two kinesins drive anterograde neuropeptide transport. Mol. Biol. Cell 28, 3542–3553. 10.1091/mbc.E16-12-0820. [PubMed: 28904207]

Author Manuscript Author Manuscript Author Manuscript Author Manuscript

Liot G, Zala D, Pla P, Mottet G, Piel M, Saudou F, 2013. Mutant Huntingtin alters retrograde transport of TrkB receptors in striatal dendrites. J. Neurosci 33, 6298–6309. 10.1523/JNEUROSCI.2033-12.2013. [PubMed: 23575829]

Littleton JT, Stern M, Schulze K, Perin M, Bellen HJ, 1993. Mutational analysis of Drosophila synaptotagmin demonstrates its essential role in ca(2+)-activated neurotransmitter release. Cell 74, 1125–1134. 10.1016/0092-8674(93)90733-7. [PubMed: 8104705]

Liu L, Tong H, Sun Y, Chen X, Yang T, Zhou G, Li X-J, Li S, 2023. Huntingtin interacting proteins and pathological implications. Int. J. Mol. Sci 24. 10.3390/ijms241713060.

Lunkes A, Lindenberg KS, Ben-Haïem L, Weber C, Devys D, Landwehrmeyer GB, Mandel J-L, Trottier Y, 2002. Proteases acting on mutant huntingtin generate cleaved products that differentially build up cytoplasmic and nuclear inclusions. Mol. Cell 10, 259–269. 10.1016/s1097-2765(02)00602-0. [PubMed: 12191472]

Malla B, Guo X, Senger G, Chasapopoulou Z, Yildirim F, 2021. A systematic review of transcriptional dysregulation in huntington's disease studied by RNA sequencing. Front. Genet 12, 751033. 10.3389/fgene.2021.751033.

Martin DDO, Ladha S, Ehrnhoefer DE, Hayden MR, 2015. Autophagy in Huntington disease and huntingtin in autophagy. Trends Neurosci. 38, 26–35. 10.1016/j.tins.2014.09.003. [PubMed: 25282404]

McGuire JR, Rong J, Li S-H, Li X-J, 2006. Interaction of huntingtin-associated protein-1 with kinesin light chain: implications in intracellular trafficking in neurons. J. Biol. Chem 281, 3552–3559. 10.1074/jbc.M509806200. [PubMed: 16339760]

Megaly M, Turgambayeva A, Hallam RD, Foran G, Megaly M, Necakov A, 2024. Human diseases associated with notch signalling: Lessions learn from Drosophila melanogaster. Front. Biosci. (Landmark Ed) 29 (6), 234. [PubMed: 38940046]

Menalled LB, Sison JD, Wu Y, Olivieri M, Li X-J, Li H, Zeitlin S, Chesselet M-F, 2002. Early motor dysfunction and striosomal distribution of huntingtin microaggregates in Huntington's disease knock-in mice. J. Neurosci 22, 8266–8276. 10.1523/JNEUROSCI.22-18-08266.2002. [PubMed: 12223581]

Michael AH, Hana TA, Mousa VG, Ormerod KG, 2024. Muscle-fiber specific genetic manipulation of Drosophila sallimus severely impacts neuromuscular development, morphology, and physiology. BioRxiv. 10.1101/2024.04.15.589595.

Milnerwood AJ, Raymond LA, 2010. Early synaptic pathophysiology in neurodegeneration: insights from Huntington's disease. Trends Neurosci. 33, 513–523. 10.1016/j.tins.2010.08.002. [PubMed: 20850189]

Mizushima N, 2010. The role of the Atg1/ULK1 complex in autophagy regulation. Curr. Opin. Cell Biol. 22, 132–139. 10.1016/j.ceb.2009.12.004. [PubMed: 20056399]

Neueder A, Landles C, Ghosh R, Howland D, Myers RH, Faull RLM, Tabrizi SJ, Bates GP, 2017. The pathogenic exon 1 HTT protein is produced by incomplete splicing in Huntington's disease patients. Sci. Rep 7, 1307. 10.1038/s41598-017-01510-z. [PubMed: 28465506]

Neueder A, Kojer K, Gu Z, Wang Y, Hering T, Tabrizi S, Taanman J-W, Orth M, 2024. Huntington's disease affects mitochondrial network dynamics predisposing to pathogenic mitochondrial DNA mutations. Brain 147, 2009–2022. 10.1093/brain/awae007. [PubMed: 38195181]

Noordermeer J, Klingensmith J, Perrimon N, Nusse R, 1994. Dishevelled and armadillo act in the wingless signalling pathway in Drosophila. Nature 367, 80–83. 10.1038/367080a0. [PubMed: 7906389]

Ochaba J, Lukacsovich T, Csikos G, Zheng S, Margulis J, Salazar L, Mao K, Lau AL, Yeung SY, Humbert S, et al. , 2014. Potential function for the Huntingtin protein as a scaffold for selective autophagy. Proc. Natl. Acad. Sci. USA 111, 16889–16894. 10.1073/pnas.1420103111. [PubMed: 25385587]

Okada Y, Yamazaki H, Sekine-Aizawa Y, Hirokawa N, 1995. The neuron-specific kinesin superfamily protein KIF1A is a unique monomeric motor for anterograde axonal transport of synaptic vesicle precursors. Cell 81, 769–780. 10.1016/0092-8674(95)90538-3. [PubMed: 7539720]

Author Manuscript Author Manuscript Author Manuscript Author Manuscript

Ormerod KG, Hadden JK, Deady LD, Mercier AJ, Krans JL, 2013. Action of octopamine and tyramine on muscles of Drosophila melanogaster larvae. J. Neurophysiol 110, 1984–1996. 10.1152/jn.00431.2013. [PubMed: 23904495]

Ormerod KG, Krans JL, Mercier AJ, 2015. Cell-selective modulation of the Drosophila neuromuscular system by a neuropeptide. J. Neurophysiol 113, 1631–1643. 10.1152/jn.00625.2014. [PubMed: 25520433]

Ormerod KG, Scibelli AE, Littleton JT, 2022. Regulation of excitation-contraction coupling at the Drosophila neuromuscular junction. J. Physiol. Lond 600, 349–372. 10.1113/JP282092. [PubMed: 34788476]

Orr HT, Zoghbi HY, 2007. Trinucleotide repeat disorders. Annu. Rev. Neurosci 30, 575–621. 10.1146/annurev.neuro.29.051605.113042. [PubMed: 17417937]

Paulson HL, Shakkottai VG, Clark HB, Orr HT, 2017. Polyglutamine spinocerebellar ataxias - from genes to potential treatments. Nat. Rev. Neurosci 18, 613–626. 10.1038/nrn.2017.92. [PubMed: 28855740]

Perlson E, Maday S, Fu M-M, Moughamian AJ, Holzbaur ELF, 2010. Retrograde axonal transport: pathways to cell death? Trends Neurosci. 33, 335–344. 10.1016/j.tins.2010.03.006. [PubMed: 20434225]

Perutz MF, Johnson T, Suzuki M, Finch JT, 1994. Glutamine repeats as polar zippers: their possible role in inherited neurodegenerative diseases. Proc. Natl. Acad. Sci. USA 91, 5355–5358. 10.1073/pnas.91.12.5355. [PubMed: 8202492]

Pircs K, Petri R, Madsen S, Brattås PL, Vuono R, Ottosson DR, St-Amour I, Hersbach BA, Matusiak-Brückner M, Lundh SH, et al. , 2018. Huntingtin aggregation impairs autophagy, leading to Argonaute-2 accumulation and global MicroRNA dysregulation. Cell Rep. 24, 1397–1406. 10.1016/j.celrep.2018.07.017. [PubMed: 30089251]

Pircs K, Drouin-Ouellet J, Horvath V, Gil J, Rezeli M, Garza R, Grassi DA, Sharma Y, St-Amour I, Harris K, et al. , 2022. Distinct subcellular autophagy impairments in induced neurons from patients with Huntington's disease. Brain 145, 3035–3057. 10.1093/brain/awab473. [PubMed: 34936701]

Podvin S, Rosenthal SB, Poon W, Wei E, Fisch KM, Hook V, 2022. Mutant huntingtin protein interaction map implicates dysregulation of multiple cellular pathways in neurodegeneration of huntington's disease. J. Huntingtons. Dis 11, 243–267. 10.3233/JHD-220538. [PubMed: 35871359]

Quarrell O, O'Donovan KL, Bandmann O, Strong M, 2012. The prevalence of juvenile Huntington's disease: A review of the literature and meta-analysis. PLoS Curr. Influenza 4, e4f8606b742ef3. 10.1371/4f8606b742ef3.

Rauskolb S, Zagrebelsky M, Dreznjak A, Deogracias R, Matsumoto T, Wiese S, Erne B, Sendtner M, Schaeren-Wiemers N, Korte M, et al. , 2010. Global deprivation of brain-derived neurotrophic factor in the CNS reveals an area-specific requirement for dendritic growth. J. Neurosci 30, 1739–1749. 10.1523/JNEUROSCI.5100-09.2010. [PubMed: 20130183]

Reiter LT, Potocki L, Chien S, Gribskov M, Bier E, 2001. A systematic analysis of human disease-associated gene sequences in Drosophila melanogaster. Genome Res. 11, 1114–1125. 10.1101/gr.169101. [PubMed: 11381037]

Riguet N, Mahul-Mellier A-L, Maharjan N, Burtscher J, Croisier M, Knott G, Hastings J, Patin A, Reiterer V, Farhan H, et al. , 2021. Nuclear and cytoplasmic huntingtin inclusions exhibit distinct biochemical composition, interactome and ultrastructural properties. Nat. Commun 12, 6579. 10.1038/s41467-021-26684-z. [PubMed: 34772920]

Rockabrand E, Slepko N, Pantalone A, Nukala VN, Kazantsev A, Marsh JL, Sullivan PG, Steffan JS, Sensi SL, Thompson LM, 2007. The first 17 amino acids of Huntingtin modulate its sub-cellular localization, aggregation and effects on calcium homeostasis. Hum. Mol. Genet 16, 61–77. 10.1093/hmg/ddl440. [PubMed: 17135277]

Romer SH, Metzger S, Peraza K, Wright MC, Jobe DS, Song L-S, Rich MM, Foy BD, Talmadge RJ, Voss AA, 2021. A mouse model of Huntington's disease shows altered ultrastructure of transverse tubules in skeletal muscle fibers. J. Gen. Physiol 153. 10.1085/jgp.202012637.

Author Manuscript Author Manuscript Author Manuscript Author Manuscript

Romero E, Cha G-H, Verstreken P, Ly CV, Hughes RE, Bellen HJ, Botas J, 2008. Suppression of neurodegeneration and increased neurotransmission caused by expanded full-length huntingtin accumulating in the cytoplasm. Neuron 57, 27–40. 10.1016/j.neuron.2007.11.025. [PubMed: 18184562]

Roos RAC, 2010. Huntington's disease: a clinical review. Orphanet J. Rare Dis. 5, 40. 10.1186/1750-1172-5-40. [PubMed: 21171977]

Ross CA, 1997. Intranuclear neuronal inclusions: a common pathogenic mechanism for glutamine-repeat neurodegenerative diseases? Neuron 19, 1147–1150. 10.1016/s0896-6273(00)80405-5. [PubMed: 9427237]

Ross CA, Aylward EH, Wild EJ, Langbehn DR, Long JD, Warner JH, Scahill RI, Leavitt BR, Stout JC, Paulsen JS, et al. , 2014. Huntington disease: natural history, biomarkers and prospects for therapeutics. Nat. Rev. Neurol 10, 204–216. 10.1038/nrneurol.2014.24. [PubMed: 24614516]

Roth JR, de Moraes RCM, Xu BP, Crawley SR, Khan MA, Melkani GC, 2023. Rapamycin reduces neuronal mutant huntingtin aggregation and ameliorates locomotor performance in Drosophila. Front. Aging Neurosci 15, 1223911. 10.3389/fnagi.2023.1223911.

Rui Y-N, Xu Z, Patel B, Chen Z, Chen D, Tito A, David G, Sun Y, Stimming EF, Bellen HJ, et al. , 2015. Huntingtin functions as a scaffold for selective macroautophagy. Nat. Cell Biol 17, 262–275. 10.1038/ncb3101. [PubMed: 25686248]

Sahl SJ, Weiss LE, Duim WC, Frydman J, Moerner WE, 2012. Cellular inclusion bodies of mutant huntingtin exon 1 obscure small fibular aggregates species. Sci. Rep 10.1038/srep00895.

Saliba SW, Vieira ELM, de Santos RPM, Candelario-Jalil E, Fiebich BL, Vieira LB, Teixeira AL, de Oliveira ACP, 2017. Neuroprotective effects of intrastriatal injection of rapamycin in a mouse model of excitotoxicity induced by quinolinic acid. J. Neuroinflammation 14, 25. 10.1186/s12974-017-0793-x. [PubMed: 28143498]

Salio C, Averill S, Priestley JV, Merighi A, 2007. Costorage of BDNF and neuropeptides within individual dense-core vesicles in central and peripheral neurons. Dev. Neurobiol 67, 326–338. 10.1002/dneu.20358. [PubMed: 17443791]

Sanyal S, 2009. Genomic mapping and expression patterns of C380, OK6 and D42 enhancer trap lines in the larval nervous system of Drosophila. Gene Expr. Patterns 9, 371–380. 10.1016/j.gep.2009.01.002. [PubMed: 19602393]

Sarkar S, Ravikumar B, Rubinsztein DC, 2009a. Autophagic clearance of aggregate-prone proteins associated with neurodegeneration. Methods Enzymol. 453, 83–110. 10.1016/S0076-6879(08)04005-6. [PubMed: 19216903]

Sarkar S, Ravikumar B, Floto RA, Rubinsztein DC, 2009b. Rapamycin and mTOR-independent autophagy inducers ameliorate toxicity of polyglutamine-expanded huntingtin and related proteinopathies. Cell Death Differ. 16, 46–56. 10.1038/cdd.2008.110. [PubMed: 18636076]

Sawada H, Ishiguro H, Nishii K, Yamada K, Tsuchida K, Takahashi H, Goto J, Kanazawa I, Nagatsu T, 2007. Characterization of neuron-specific huntingtin aggregates in human huntingtin knock-in mice. Neurosci. Res 57, 559–573. 10.1016/j.neures.2007.01.002. [PubMed: 17335925]

Schiefer J, Werner CJ, Reetz K, 2015. Clinical diagnosis and management in early Huntington's disease: a review. Degener. Neurol. Neuromuscul. Dis 5, 37–50. 10.2147/DNND.S49135. [PubMed: 32669911]

Sharp AH, Loev SJ, Schilling G, Li SH, Li XJ, Bao J, Wagster MV, Kotzuk JA, Steiner JP, Lo A, 1995. Widespread expression of Huntington's disease gene (IT15) protein product. Neuron 14, 1065–1074. 10.1016/0896-6273(95)90345-3. [PubMed: 7748554]

Slow EJ, van Raamsdonk J, Rogers D, Coleman SH, Graham RK, Deng Y, Oh R, Bissada N, Hossain SM, Yang Y-Z, et al. , 2003. Selective striatal neuronal loss in a YAC128 mouse model of Huntington disease. Hum. Mol. Genet 12, 1555–1567. 10.1093/hmg/ddg169. [PubMed: 12812983]

Smith EJ, Sathasivam K, Landles C, Osborne GF, Mason MA, Gomez-Paredes C, Taxy BA, Milton RE, Ast A, Schindler F, et al. , 2023. Early detection of exon 1 huntingtin aggregation in zQ175 brains by molecular and histological approaches. Brain Commun. 5, fcad010. 10.1093/braincomms/fcad010.

Author Manuscript Author Manuscript Author Manuscript Author Manuscript

Stjepanovic G, Davies CW, Stanley RE, Ragusa MJ, Kim DJ, Hurley JH, 2014. Assembly and dynamics of the autophagy-initiating Atg1 complex. Proc. Natl. Acad. Sci. USA 111, 12793–12798. 10.1073/pnas.1407214111. [PubMed: 25139988]

Szebenyi G, Morfini GA, Babcock A, Gould M, Selkoe K, Stenoien DL, Young M, Faber PW, MacDonald ME, McPhaul MJ, et al. , 2003. Neuropathogenic forms of huntingtin and androgen receptor inhibit fast axonal transport. Neuron 40, 41–52. 10.1016/s0896-6273(03)00569-5. [PubMed: 14527432]

Tabrizi SJ, Schobel S, Gantman EC, Mansbach A, Borowsky B, Konstantinova P, Mestre TA, Panagoulias J, Ross CA, Zauderer M, et al. , 2022. A biological classification of Huntington's disease: the integrated staging system. Lancet Neurol. 21, 632–644. 10.1016/S1474-4422(22)00120-X. [PubMed: 35716693]

Tagawa K, Hoshino M, Okuda T, Ueda H, Hayashi H, Engemann S, Okado H, Ichikawa M, Wanker EE, Okazawa H, 2004. Distinct aggregation and cell death patterns among different types of primary neurons induced by mutant huntingtin protein. J. Neurochem 89, 974–987. 10.1111/j.1471-4159.2004.02372.x. [PubMed: 15140196]

The Huntington''s Disease Collaborative Research Group, 1993. A novel gene containing a trinucleotide repeat that is expanded and unstable on Huntington's disease chromosomes. The Huntington's Disease Collaborative Research Group. Cell 72, 971–983. 10.1016/0092-8674(93)90585-e. [PubMed: 8458085]

Tourette C, Li B, Bell R, O'Hare S, Kaltenbach LS, Mooney SD, Hughes RE, 2014. A large scale huntingtin protein interaction network implicates rho GTPase signaling pathways in Huntington disease. J. Biol. Chem 289, 6709–6726. 10.1074/jbc.M113.523696. [PubMed: 24407293]

Trushina E, Dyer RB, Badger JD, Ure D, Eide L, Tran DD, Vrieze BT, Legendre-Guillemin V, McPherson PS, Mandavilli BS, et al. , 2004. Mutant huntingtin impairs axonal trafficking in mammalian neurons in vivo and in vitro. Mol. Cell. Biol 24, 8195–8209. 10.1128/MCB.24.18.8195-8209.2004. [PubMed: 15340079]

Van Raamsdonk JM, Murphy Z, Slow EJ, Leavitt BR, Hayden MR, 2005. Selective degeneration and nuclear localization of mutant huntingtin in the YAC128 mouse model of Huntington disease. Hum. Mol. Genet 14, 3823–3835. 10.1093/hmg/ddi407. [PubMed: 16278236]

Vasin A, Zueva L, Torrez C, Volfson D, Littleton JT, Bykhovskaia M, 2014. Synapsin regulates activity-dependent outgrowth of synaptic boutons at the Drosophila neuromuscular junction. J. Neurosci 34, 10554–10563. 10.1523/JNEUROSCI.5074-13.2014. [PubMed: 25100589]

Waldvogel HJ, Kim EH, Tippett LJ, Vonsattel J-PG, Faull RLM, 2015. The neuropathology of huntington's disease. Curr. Top. Behav. Neurosci 22, 33–80. 10.1007/7854_2014_354. [PubMed: 25300927]

Walker FO, 2007. Huntington's disease. Lancet 369, 218–228. 10.1016/S0140-6736(07)60111-1. [PubMed: 17240289]

Weiss KR, Littleton JT, 2016. Characterization of axonal transport defects in Drosophila huntingtin mutants. J. Neurogenet 30, 212–221. 10.1080/01677063.2016.1202950. [PubMed: 27309588]

Weiss KR, Kimura Y, Lee W-CM, Littleton JT, 2012. Huntingtin aggregation kinetics and their pathological role in a Drosophila Huntington's disease model. Genetics 190, 581–600. 10.1534/genetics.111.133710. [PubMed: 22095086]

Wellington CL, Ellerby LM, Hackam AS, Margolis RL, Trifiro MA, Singaraja R, McCutcheon K, Salvesen GS, Propp SS, Bromm M, et al. , 1998. Caspase cleavage of gene products associated with triplet expansion disorders generates truncated fragments containing the polyglutamine tract. J. Biol. Chem 273, 9158–9167. 10.1074/jbc.273.15.9158. [PubMed: 9535906]

Wellington CL, Singaraja R, Ellerby L, Savill J, Roy S, Leavitt B, Cattaneo E, Hackam A, Sharp A, Thornberry N, et al. , 2000. Inhibiting caspase cleavage of huntingtin reduces toxicity and aggregate formation in neuronal and nonneuronal cells. J. Biol. Chem 275, 19831–19838. 10.1074/jbc.M001475200. [PubMed: 10770929]

Wright GEB, Collins JA, Kay C, McDonald C, Dolzhenko E, Xia Q, Bečanović K, Drögemöller BI, Semaka A, Nguyen CM, et al. , 2019. Length of uninterrupted CAG, independent of polyglutamine size, results in increased somatic instability, hastening onset of Huntington disease. Am. J. Hum. Genet 104, 1116–1126. 10.1016/j.ajhg.2019.04.007. [PubMed: 31104771]

Author Manuscript Author Manuscript Author Manuscript Author Manuscript

Yang H, Yang S, Jing L, Huang L, Chen L, Zhao X, Yang W, Pan Y, Yin P, Qin ZS, et al. , 2020. Truncation of mutant huntingtin in knock-in mice demonstrates exon1 huntingtin is a key pathogenic form. Nat. Commun 11, 2582. 10.1038/s41467-020-16318-1. [PubMed: 32444599]

Yoshihara M, Littleton JT, 2002. Synaptotagmin I functions as a calcium sensor to synchronize neurotransmitter release. Neuron 36, 897–908. 10.1016/s0896-6273(02)01065-6. [PubMed: 12467593]

Yu Z-X, Li S-H, Evans J, Pillarisetti A, Li H, Li X-J, 2003. Mutant huntingtin causes context-dependent neurodegeneration in mice with Huntington's disease. J. Neurosci 23, 2193–2202. 10.1523/JNEUROSCI.23-06-02193.2003. [PubMed: 12657678]

Zheng Z, Li A, Holmes BB, Marasa JC, Diamond MI, 2013. An N-terminal nuclear export signal regulates trafficking and aggregation of Huntingtin (Htt) protein exon 1. J. Biol. Chem 288, 6063–6071. 10.1074/jbc.M112.413575. [PubMed: 23319588]

Author Manuscript
Author Manuscript
Author Manuscript
Author Manuscript

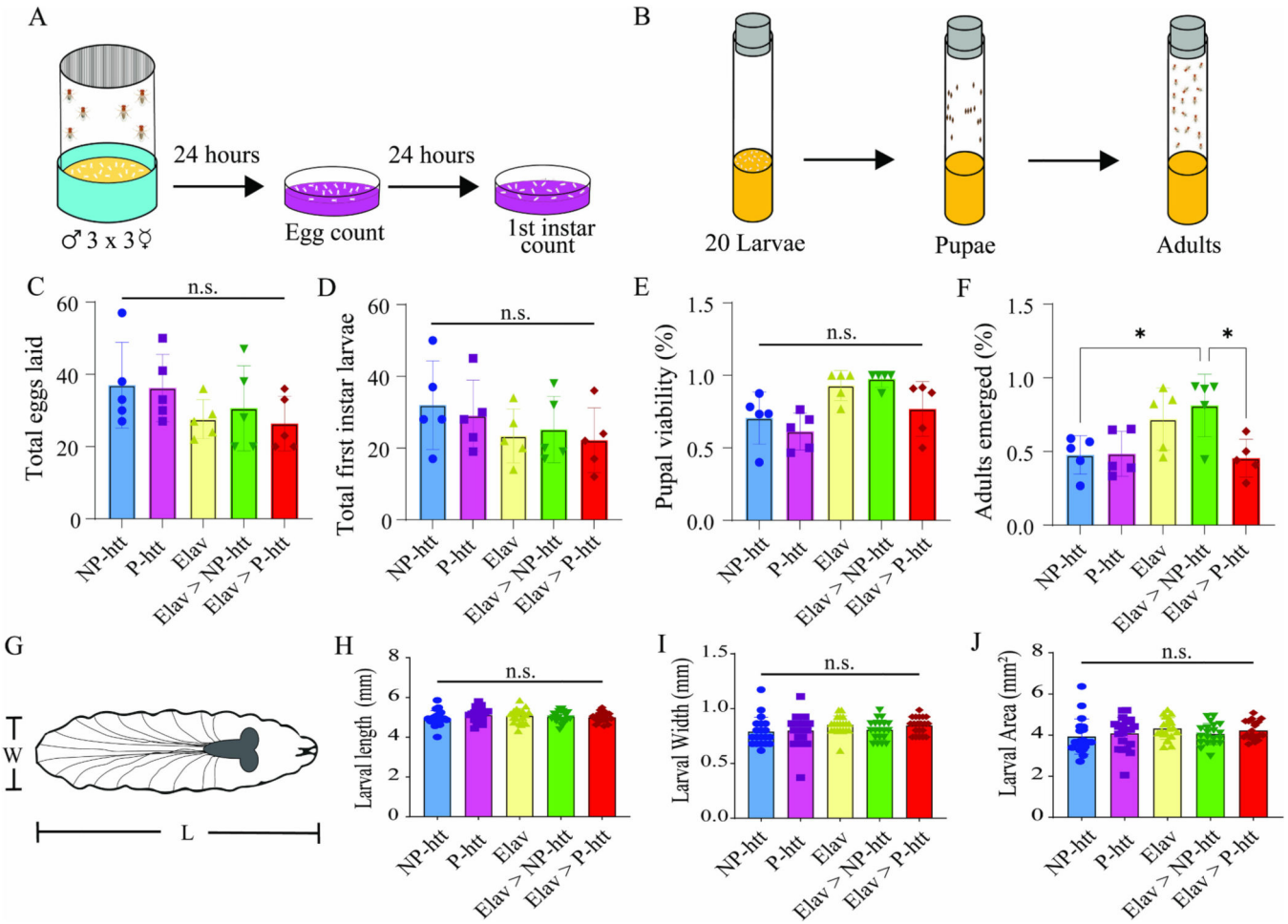

Fig. 1. Pathogenic htt protein aggregation does not impact larval morphology or development.

A. Diagram of egg laying assay. Eggs were collected from a cross between 3 males and 3 females after 24 h and emerging first-instar larvae were collected 24 h afterwards. **B.** Diagram of larval development assay. 20 larvae were transferred onto food vials and tracked until pupation and adulthood. No significant differences were observed from the 5 different genotypes investigated from the total eggs laid **(C),** total first instar larvae counted **(D)** or pupal viability **(E). F.** Percentage of adults that emerged from each crossed showed significant differences. **G.** A schematic depicting a third-instar larva being measured for length and width. No significant differences were found in larval length **(H)**, width **(I)**, or area **(J)** across the 5 genotypes investigated. * indicates $P > 0.05$ from a One-way ANOVA.

Author Manuscript
Author Manuscript
Author Manuscript
Author Manuscript

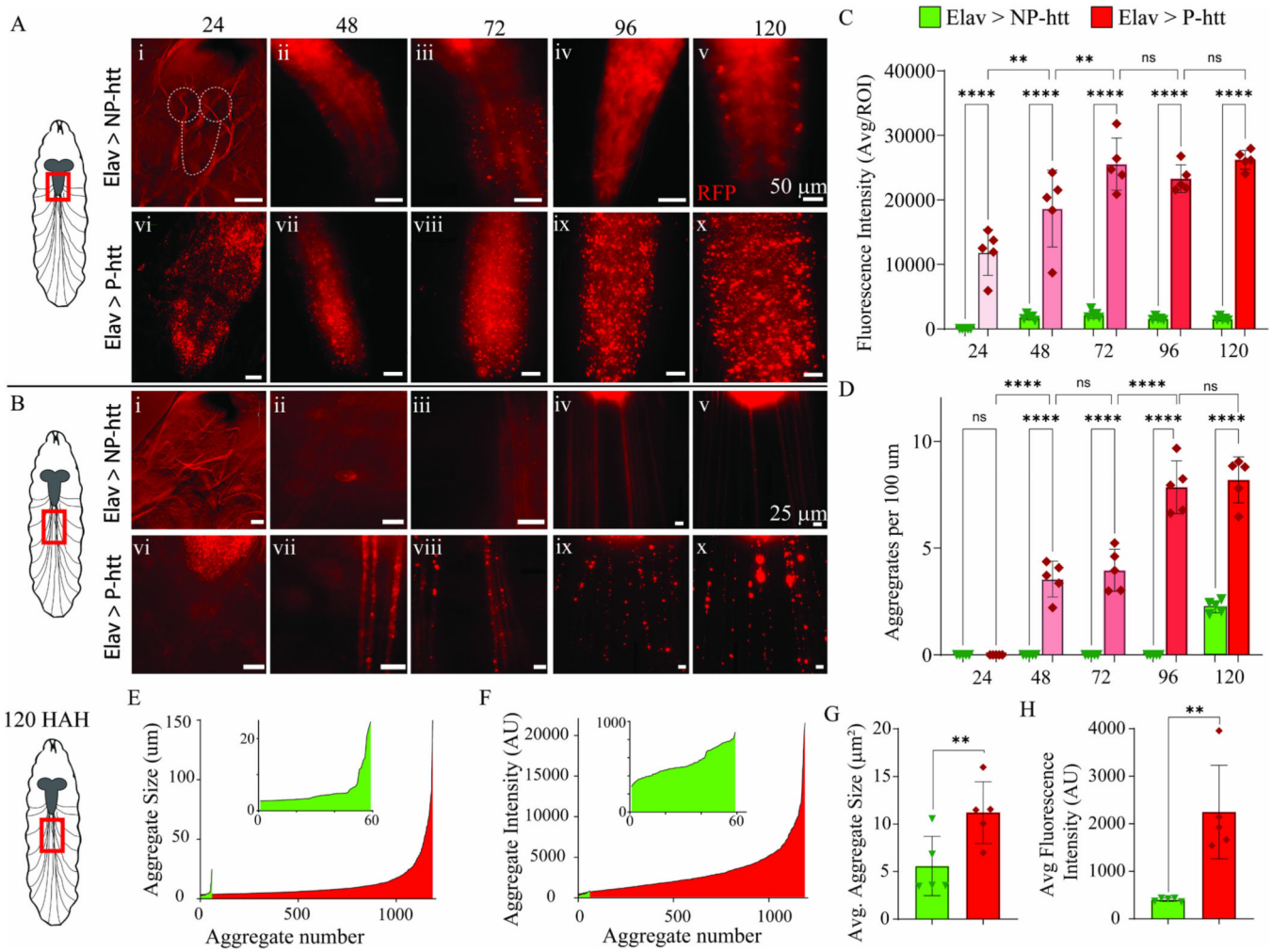

Fig. 2. Expanding the PolyQ repeat region causes a progressive proliferation of htt aggregates throughout larval development.

A. *Left:* Schematic depicting site of imaging on a third-instar larva. Intravital images (24, 48, 72 Hours after Hatching) and dissected preparations (96 and 120 Hours after Hatching) of Ventral Nerve Cords (VNC). First row: representative images of larvae expressing Elav>NP-*htt* from each time point. Second row: representative images of Elav>P-*htt* from each time point. Scale bar: 50 µm. **B**. *Left:* Schematic depicting site of imaging on a third-instar larva. Intravital images (24, 48, 72 Hours after Hatching) and dissected preparations (96 and 120 Hours after Hatching) of segmental nerve branches (SNB). First row: representative images from Elav>NP-*htt* at each time point. Second row: representative images from Elav>P-*htt* at each time point. Scale bar: 25 µm. **C.** Average RFP Fluorescence intensity (AU) from the VNC for larvae expressing Elav>NP-*htt vs* Elav>P-*htt* across all five timepoints imaged. **D.** Average number of RFP aggregates per 100 µm of SNB for larvae expressing Elav>NP-*htt vs* Elav>NP-*htt* across all five timepoints imaged. ***E*-H:** Data from 120 HAH larvae. **E.** Average RFP aggregate size (µm) of all aggregates of 120 HAH larvae in Elav>NP-*htt* (green) *vs* Elav>P-*htt* (red). Inset: Elav > NP-htt only. **F.** Average RFP Fluorescence intensity (AU) of all aggregates of 120 HAH larvae between Elav>NP-*htt* (green) *vs* Elav>P-*htt* (red). Inset: Elav > NP-htt only. **G.** Average aggregate size of 120

Author Manuscript Author Manuscript Author Manuscript Author Manuscript

HAH larvae in Elav>NP-*htt vs* Elav>P-*htt*. **H.** Average aggregate fluorescence intensity (AU) of 120 HAH larvae between Elav>NP-*htt* and Elav>P-*htt.* * indicates P > 0.05, ** $P > 0.01$, *** $P > 0.001$, **** $P > 0.0001$ from a One-way ANOVA. (For interpretation of the references to colour in this figure legend, the reader is referred to the web version of this article.)

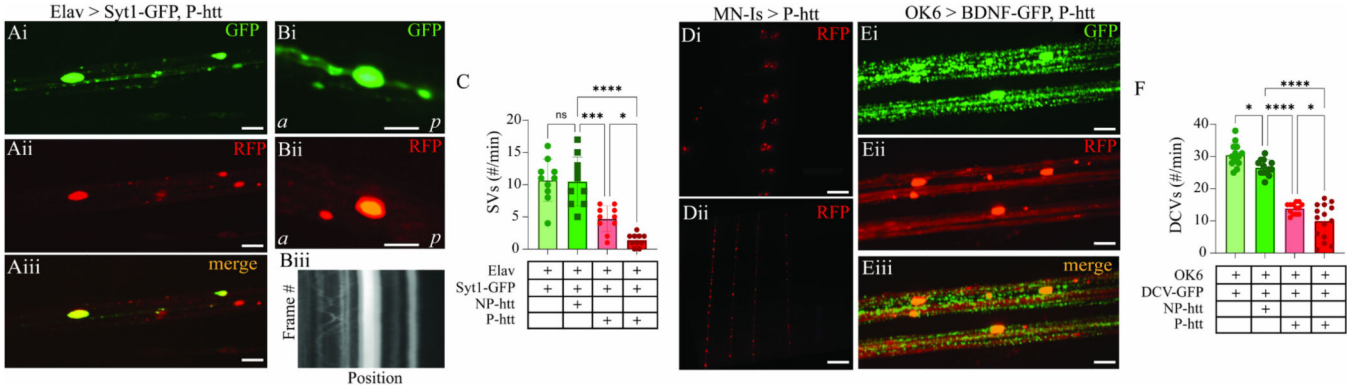

Fig. 3. Htt aggregates cause significant trafficking deficits of synaptic vesicles and dense core vesicles.

Ai-iii. Confocal microscopy images of Elav > Syt1-GFP, P-htt from a segmental nerve branch. Scale bar: 10 μm. **Bi-ii.** Confocal microscopy image of individual htt-aggregate from Elav > Syt1-GFP, htt-P. Scale bar: 5 μm. **Biii.** Kymograph of Syt1-GFP SVs from Bi, highlighting differences in mobility up-and down-stream of aggregate. *a:* anterior/upstream, *p:* posterior/downstream. **C.** Quantification of SV flux (#/min). Genotypes are indicated below figure, + indicates presence of genetic element. Light red: quantification upstream of aggregate, Dark red bar: quantification downstream of aggregate. **Di-Dii.** Fluorescence microscopy image of MN-Is > P-htt in the **(Di**) VNC and (**Dii**) SNBs. Scale bar: 50 μm (Di), 25 μm (Dii). **Ei-iii.** Confocal microscopy images of OK6 > BDNF-GFP, P-htt from a segmental nerve branch. Scale bar: 10 μm. **F.** Quantification of dense core vesicle flux (#/min). Genotypes are indicated below figure, + indicates presence of genetic element. Light red: quantification upstream of aggregate, Dark red bar: quantification downstream of aggregate. * indicates P > 0.05, ** P > 0.01, *** P > 0.001, **** P > 0.0001 from a One-way ANOVA. (For interpretation of the references to colour in this figure legend, the reader is referred to the web version of this article.)

Author Manuscript Author Manuscript Author Manuscript Author Manuscript

Author Manuscript Author Manuscript Author Manuscript Author Manuscript

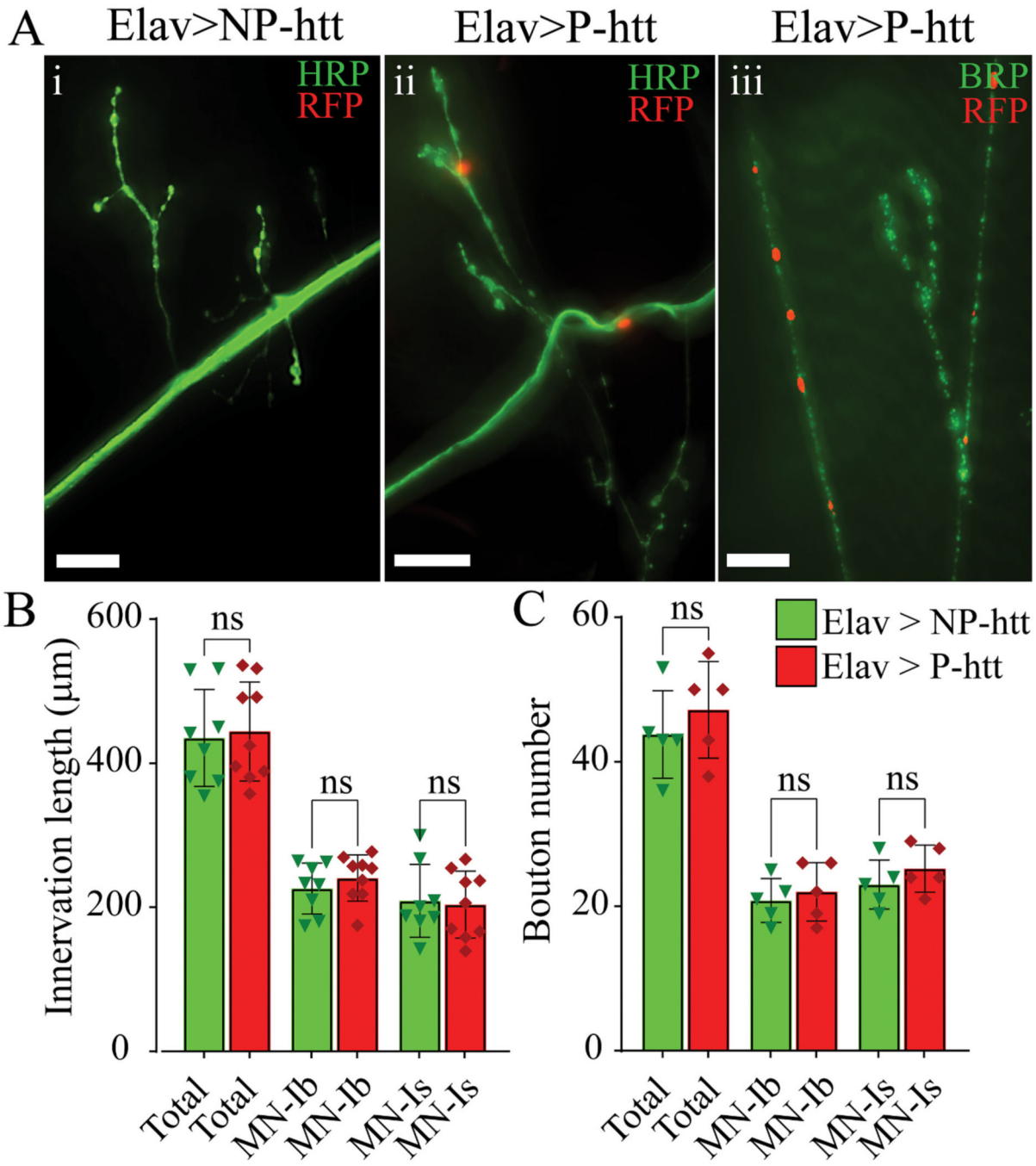

Fig. 4. Htt-aggregation does not impact larval NMJ morphology.

A. Immunohistochemical stain from **i.** Elav-Gal4 > NP-htt and **ii:** Elav-Gal4 > P-htt using horseradish peroxidase (HRP) and red fluorescent protein (RFP). **Aiii.** Immunostain of Elav-Gal4 > UAS-htt-Q138 for bruchpilot (brp) and RFP. Scale bar: 50 μm. **B.** The total innervation length of motor neurons (MNs) along the surface of muscle fiber 4 was quantified for both Elav > P-*htt* and Elav > NP-*htt*. The MNs were further divided into the MN-Ib and MN-Is subtypes. **C.** Total bouton number along the survive of MF4 was quantified for both Elav > P-*htt* and Elav > NP-*htt*. The bouton numbers were further

divided assessed by associating them to either MN-Ib or MN-Is subtypes. (For interpretation of the references to colour in this figure legend, the reader is referred to the web version of this article.)

Author Manuscript Author Manuscript Author Manuscript Author Manuscript

Author Manuscript Author Manuscript Author Manuscript Author Manuscript

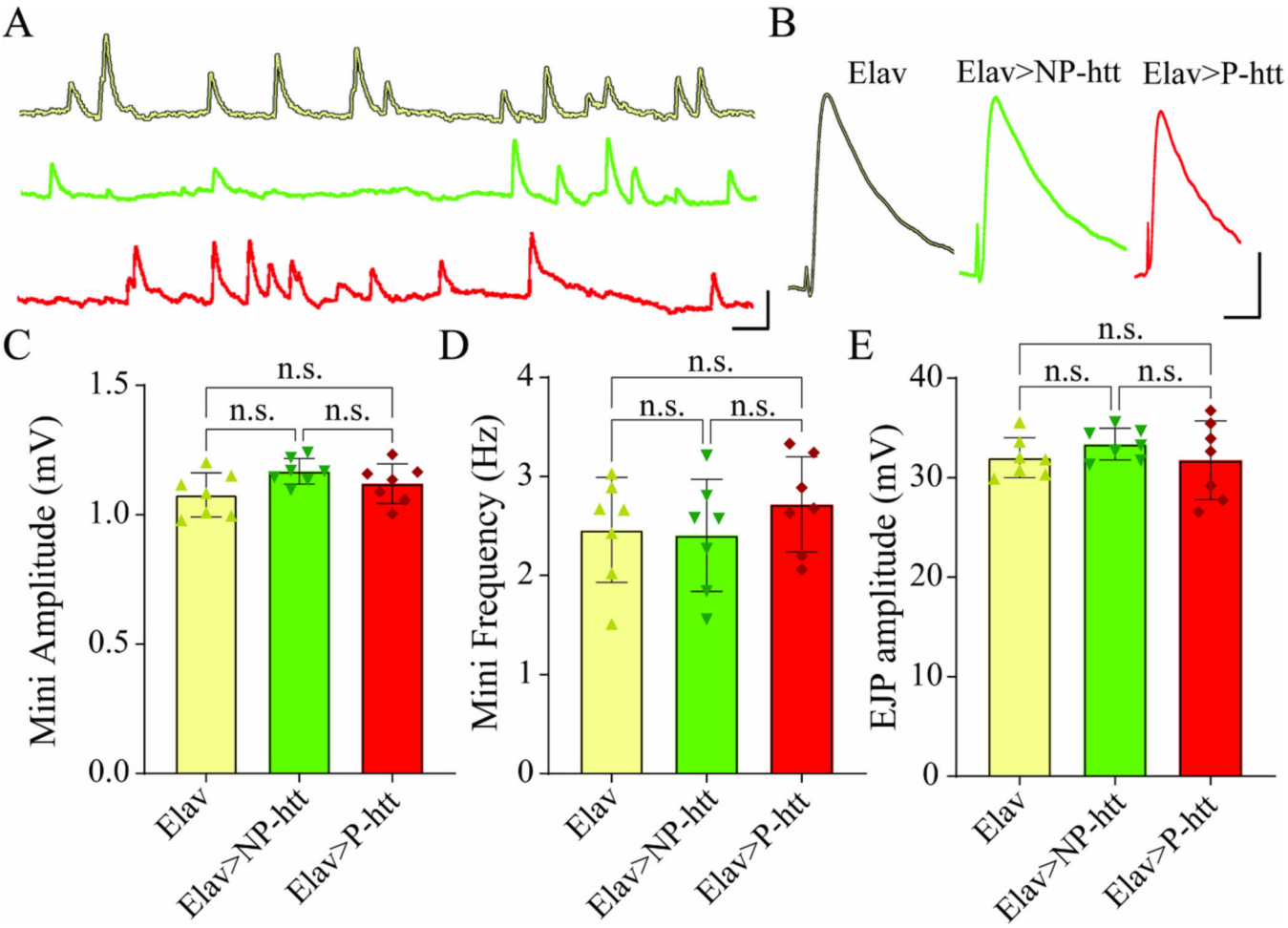

Fig. 5. Htt aggregation in motor neurons does not significantly impact NMJ transmission.

A. Representative trace of Miniature excitatory post junction potentials (MINI) from Elav (yellow), Elav>NP-htt (Yellow), and Elav>P-htt (red). Scale bars: 1 mV, 5 ms. **B.** Representative trace of excitatory post junction potentials (EJP) from Elav (yellow), Elav>NP-htt (Yellow), and Elav>P-htt (red). Scale bars: 15 mV, 20 ms. **C.** MINI amplitude (mV) of Elav (Elav), Elav>NP-htt (NP), and Elav>P-htt (P). **D.** MINI frequency (Hz) for of Elav (Elav), Elav>NP-htt (NP), and Elav>P-htt (P). **E.** EJP amplitude (mV) of Elav (Elav), Elav>NP-htt (NP), and Elav>P-htt (P). (For interpretation of the references to colour in this figure legend, the reader is referred to the web version of this article.)

Author Manuscript Author Manuscript Author Manuscript Author Manuscript

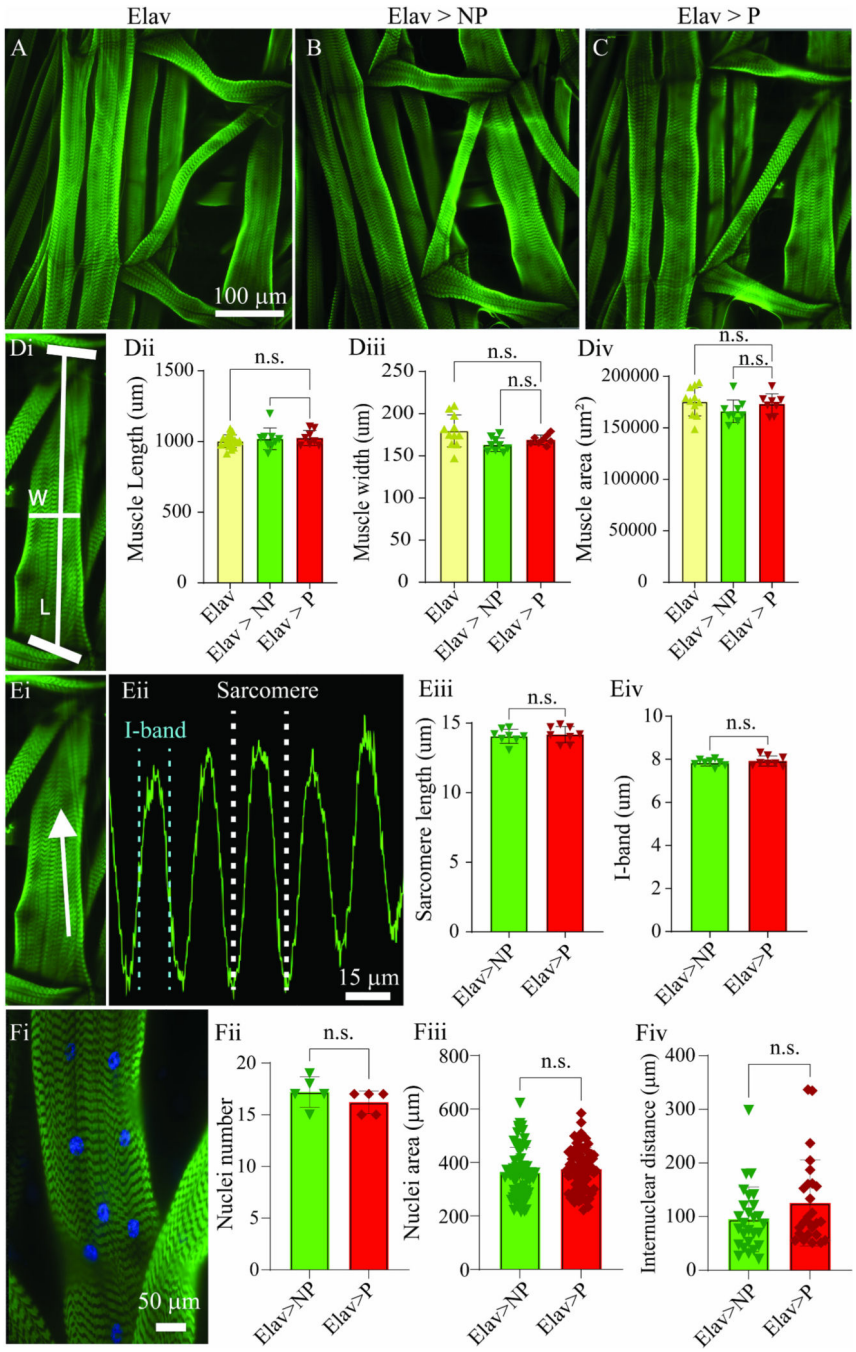

Fig. 6. Htt-aggregation does not impact muscle ultrastructure.

Immunostain using phalloidin (actin) of an abdominal hemisegment highlighting longitudinal muscles 4, 5, 6, 7, 12, and 13 from **A.** Elav, **B.** Elav > NP-htt, and **C.** Elav > P-htt. Scale bar: 100 µm. **Di.** Immunostain of MF12 demonstrating how muscle width (W) and length (L) measurements were obtained. Quantification of gross muscle length (**Dii**), width (**Diii**), and area (**Div**) for Elav, Elav > NP-htt, and Elav > P-htt. **Ei.** Immunostain of MF12 showing how muscle ultrastructure was determined using a fluorescence line plot. Along white arrow indicates the location and direction of ultrastructural analysis. **Eii.**

Author Manuscript Author Manuscript Author Manuscript Author Manuscript

Fluorescence intensity profile line for GFP (actin). Dashed white and teal lines indicate how sarcomere and I-band measurements were calculated respectively. Scale bar: 15 μm. Quantification for muscle (**Eiii)** I-band length and (**Eiv**) sarcomere length measurements from Elav > NP-htt, and Elav > P-htt. **Fi.** Immunostain for MF12 with phalloidin and DAPI. Scale bar: 50 μm. Quantification of nuclei number (**Fii**), nuclei area (**Fiii**), and internuclear distance (**Fiv**) from Elav > NP-htt, and Elav > P-htt. (For interpretation of the references to colour in this figure legend, the reader is referred to the web version of this article.)

Author Manuscript Author Manuscript Author Manuscript Author Manuscript

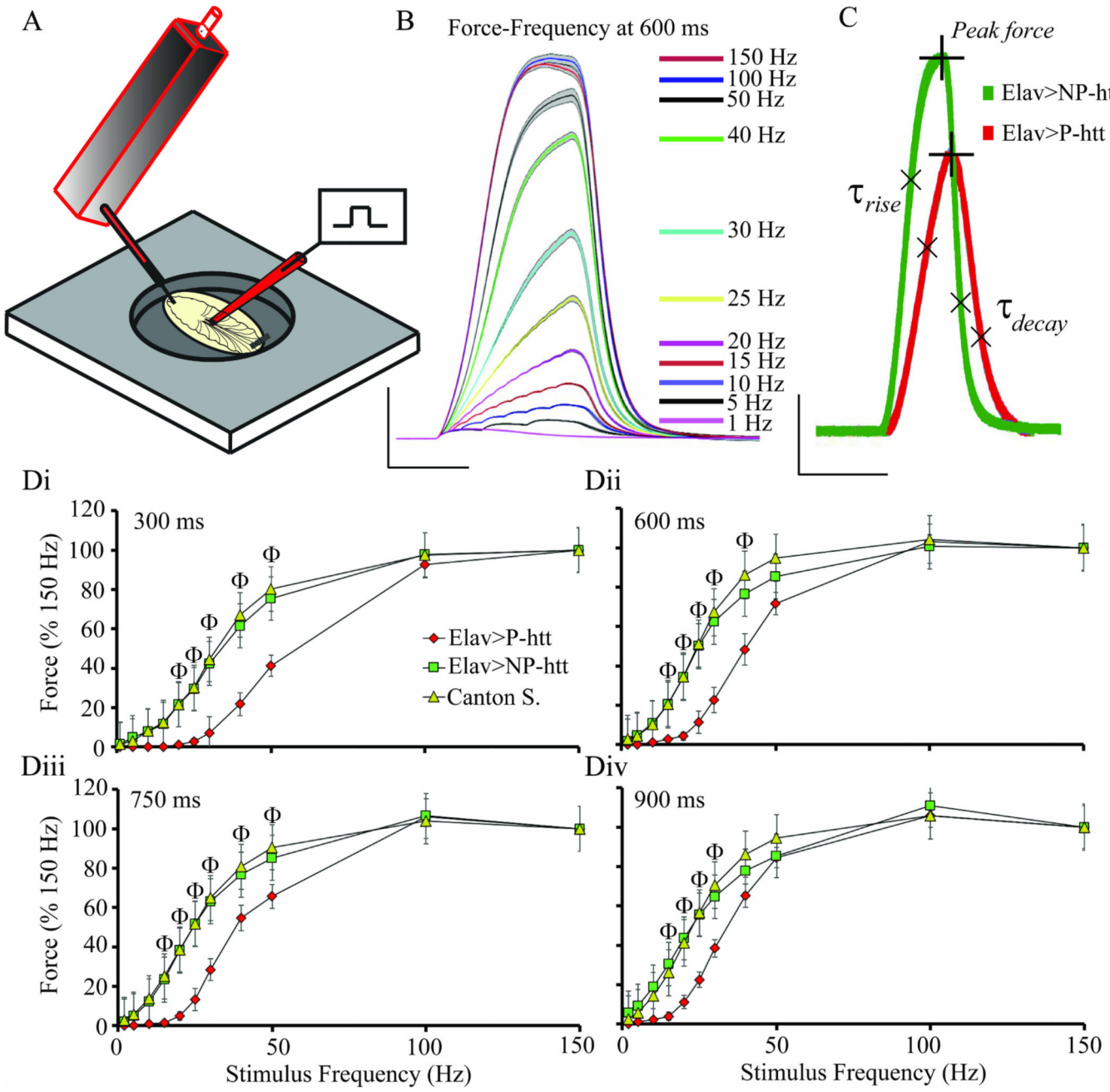

Fig. 7. P-htt expression in motor neurons significantly reduces neuromuscular transduction.

A. Schematic of larval force transducer setup. **B.** Representative force-frequency recordings from third-instar larvae. Six replicate contractions from each of the 11 stimulation frequencies were averaged and plotted with a 95 % confidence interval. **C.** Representative traces from Canton S. control and P-htt larvae with peak force, rise- and decay-tau (**τ**) shown. Scale bars: 1mN, 750 ms. **D.** Force-frequency plots for 4 different stimulation durations 300 ms (Di), 600 ms (Dii), 750 ms (Diii), 900 ms (Div). **Φ:** indicates significant differences between Elav>NP-htt and Elav > P-htt.

Author Manuscript Author Manuscript Author Manuscript Author Manuscript

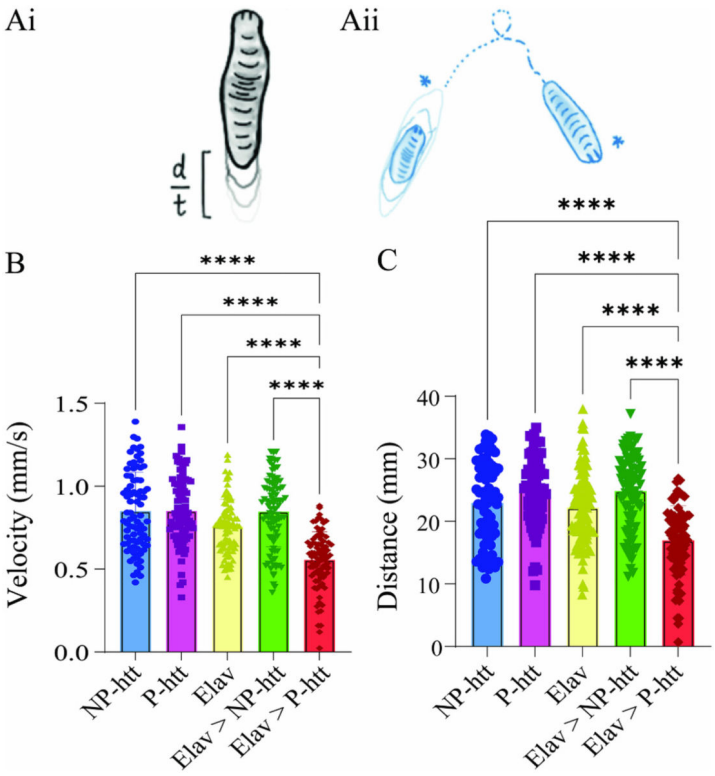

Fig. 8. Pathogenic htt-expression in the NS significantly impacts larval crawling.

A. Schematic depicting different crawling patterns quantified: velocity (i) and distance (ii). **B.** Velocity (mm/s) is significantly decreased in Elav > P-htt compared to Elav > NP-htt and all controls. **C.** Distance travelled (mm) over 30 s is significantly decreased in Elav > P-htt compared to Elav > NP-htt and all controls. * indicates $P > 0.05$, ** $P > 0.01$, *** $P > 0.001$, **** $P > 0.0001$ from a One-way ANOVA.

Author Manuscript Author Manuscript Author Manuscript Author Manuscript

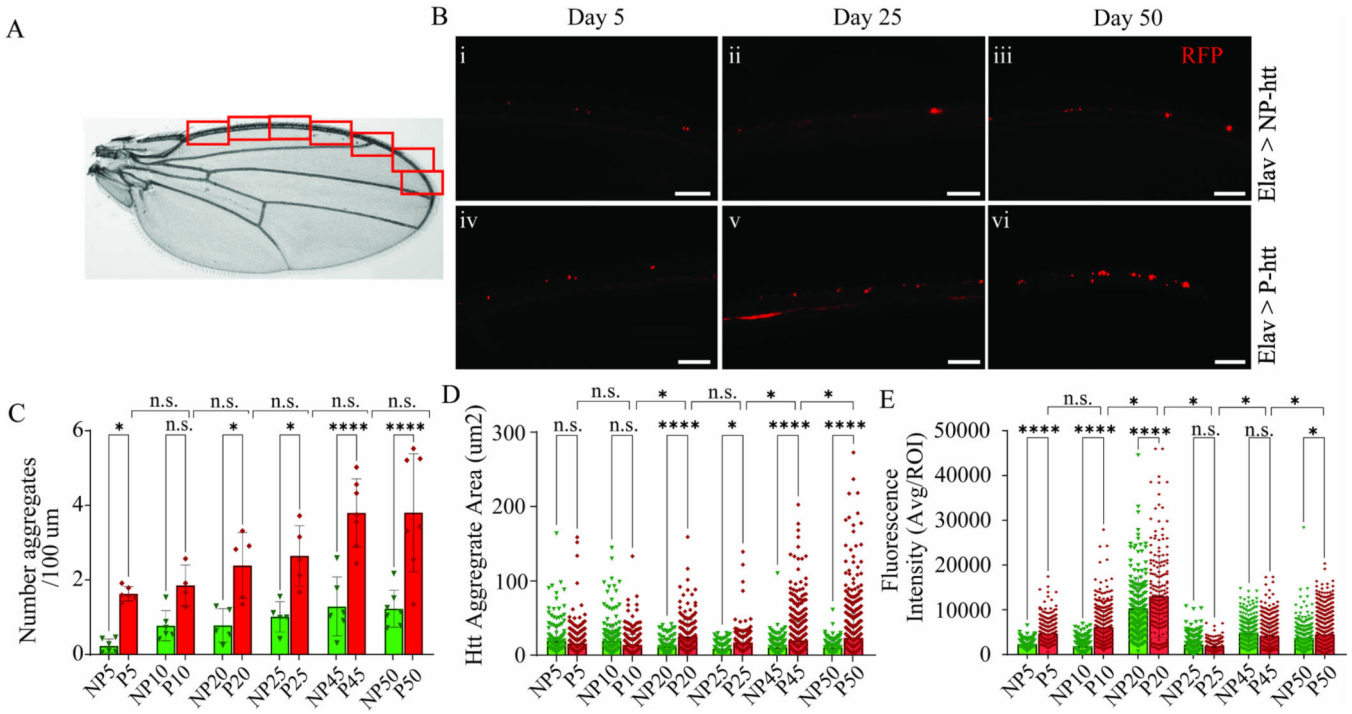

Fig. 9. Modeling htt-aggregation in the adult wing reveals significant increases in the number and size of aggregates from flies expressing pathogenic htt.

A. Bright-field microscope image of an adult *Drosophila* wing, highlighting the location of images along the L1 vein in red boxes. Scale bar: 50 μm. B. Fluorescence microscopy images from the wings of Elav > NP-htt (Bi-iii) and Elav > P-htt (Biv-vi) from 3 time points, day 5, 25, and 50. Scale bar: 50 μm. Quantification of the (C) number of aggregates per 100 μm, (D) aggregate area, and (E) fluorescence intensity from Elav > NP-htt and Elav > P-htt. * indicates P > 0.05, ** P > 0.01, *** P > 0.001, **** P > 0.0001 from a One-way ANOVA. (For interpretation of the references to colour in this figure legend, the reader is referred to the web version of this article.)

Author Manuscript Author Manuscript Author Manuscript Author Manuscript

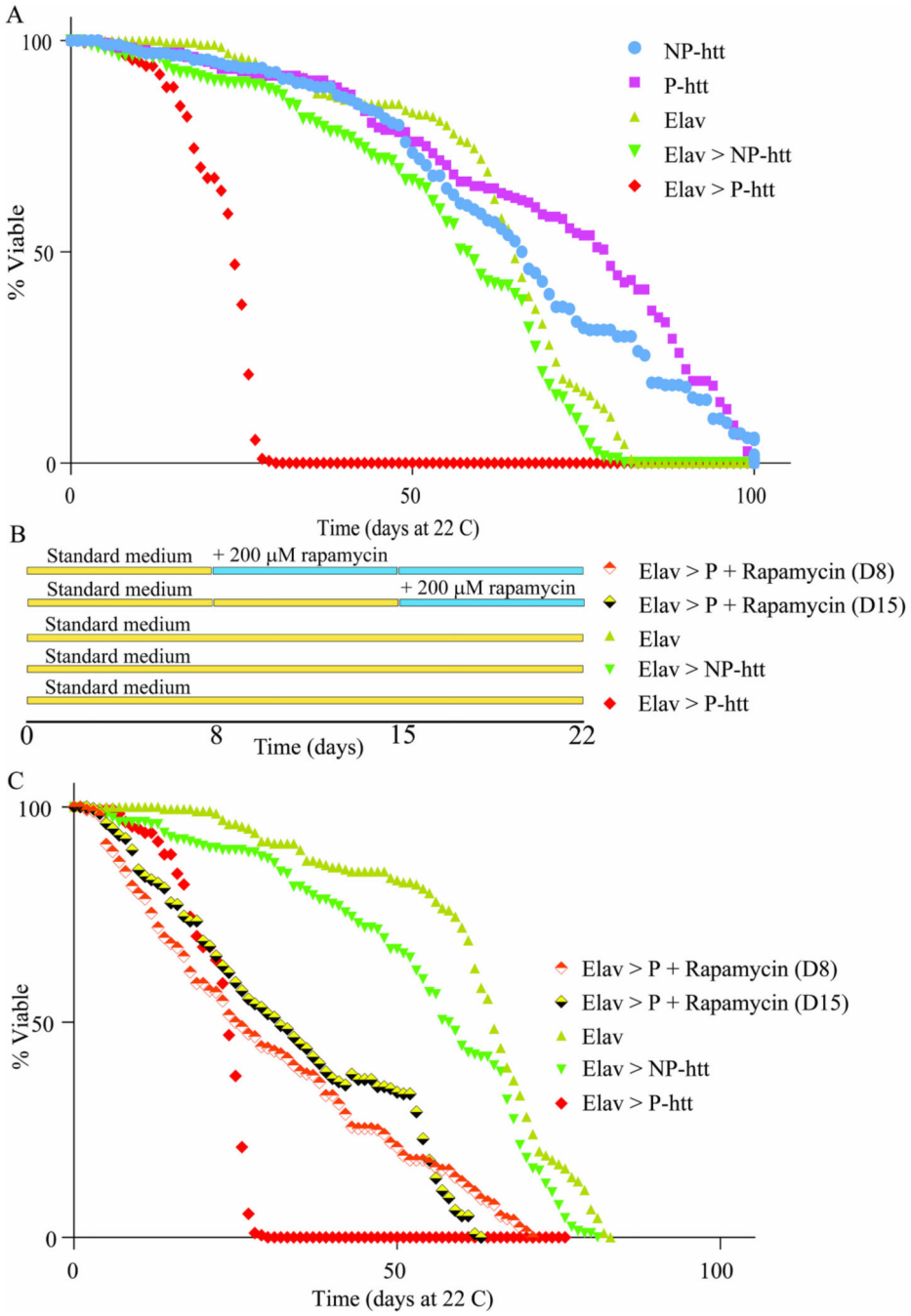

Fig. 10. Expression of htt aggregates significantly reduces adult lifespan, which is partially rescued with rapamycin feeding.

Lifespan (% viability) was tracked for adults reared at 22 °C for 5 different genotypes plotted as a function of time in days. **B.** Schematic showing the feeding schedule of rapamycin for the experiments in C. **C.** Lifespan (% viability) was tracked for adults reared in 22 °C for 3 different genotypes and Elav > P-htt fed standard medium supplemented with 200 µM rapamycin 8 days (D8) and 15 days (D15) post eclosion.

Author Manuscript Author Manuscript Author Manuscript Author Manuscript

Table 1

Fly lines, genotypes, and abbreviations used throughout investigation.

Full genotype	Abbreviation	BDSC Stock #	Reference
UAS- HttQ15-mRFP/ +	NP-htt	–	(Weiss and Littleton, 2016; Weiss et al., 2012)
UAS- HttQ138-mRFP/+	P-htt	–	(Weiss and Littleton, 2016; Weiss et al., 2012)
Elav-Gal4/+	Elav	458	(Noordermeer et al., 1994)
Elav-Gal4/+; UAS- HttQ15-mRFP/+	Elav > NP-htt	–	(Weiss and Littleton, 2016; Weiss et al., 2012)
Elav-Gal4/+; UAS- HttQ138-mRFP/+	Elav > P-htt	–	(Weiss and Littleton, 2016; Weiss et al., 2012)
OK6-Gal4/+	OK6	64,199	(Sanyal, 2009)
UAS-Syt1-GFP/+	Syt1-GFP	–	
UAS-BDNF-GFP/+	BDNF-GFP	–	
UAS-Mito-GFP	Mito-GFP	95,270	(Cox and Spradling, 2003)
Canton. S.	Canton. S.	6365	(Hoskins et al., 2001)
Motor Neuron Is-Gal4	MN-Is	–	(Aponte-Santiago et al., 2020)
Motor Neuron Ib-Gal4	MN-Ib	40,701	(Aponte-Santiago et al., 2020)
appl-Gal4	appl	32,040	(Fang et al., 2013)